The depths and thicknesses of the magma bodies that fed some of the largest Quaternary eruptions on Earth

Guilherme A. R. Gualda, Vanderbilt University, Nashville, TN, USA (Corresponding author)

Bradley W. Pitcher, University of Delaware, Newark, DE, USA

Sarah L. Smithies, University of Canterbury, Christchurch, New Zealand

Lydia J. Harmon, Occidental College, Los Angeles, CA, USA

Ayla S. Pamukçu, Stanford University, Stanford, CA, USA

Manuscript submitted to
Bulletin of Volcanology

Abstract

Volcanic systems are critical for the evolution and dynamics of the Earth; yet, our understanding of the plumbing systems that feed eruptions is hampered by our inability to directly observe magmas at depth. We present a compilation of matrix-glass data and rhyolite-MELTS pre-eruptive storage pressures for eleven Quaternary VEI 6+ caldera-forming eruptions worldwide with volumes ranging from 35 to 1,500 km^3, and we assess the depths and thicknesses of the magma bodies that fed these eruptions. We show that magmas that feed VEI 6+ eruptions are typically stored at median depths of 3.4-5.1 km, with magma body thicknesses typically in the range of 1.5 to 4 km. Two smaller eruptions (i.e., < 50 km^3) in the TVZ were fed from magmas stored at deeper levels (~10-12 km) and are characterized by much smaller calculated thicknesses (≤ 1.5 km), which may be facilitated by the extensional tectonic environment and their eruption during the early stages of magmatic cycles. In combination, results suggest that the interval between 3 and 5 km depth in the shallow crust is the most favorable for the accumulation of large volumes of magma. Comparison of thicknesses calculated using geobarometry with volume:area values shows that most magmas that feed VEI 6+ eruptions are found in melt-dominated magma bodies, rather than fed by mobilization of melt dispersed in magma mush on eruption timescales. Finally, magma thickness is constant as a function of volume for volumes > 200 km^3, which implies growth of magma bodies that feed supereruptions via lateral spreading. The characteristics outlined above suggest that the behavior of magmatic systems shifts when magma volume reaches ~200 km^3.

Keywords

rhyolite; volcanic eruptions; supereruptions; magma bodies; magmatism

1. Introduction

Volcanic systems play a critical role in the evolution and dynamics of the Earth, and they are societally important due to the hazards they pose and the economic resources they can generate and sustain. Yet, our understanding of magmatic systems is hampered by our inability to directly observe the processes taking place several kilometers below the Earth's surface and on timescales much longer than the human lifespan. Geophysical evidence is often used to infer the distribution of material properties within the crust (Huang et al. 2015; Delph et al. 2017; Biondi et al. 2023; Duan et al. 2025), including the distribution and crystal content of magmas at depth – however, there are limits to what can be imaged geophysically, and we are constrained to observing magmatic systems in their current configuration. Alternatively, we can use modeling to understand the potential distribution of magmas within the crust (Jellinek and DePaolo 2003; Karlstrom et al. 2010; Bachmann and Huber 2016, 2019), but such models are typically limited to outlining possible outcomes, rather than providing information on the properties and processes that characterize specific magmatic systems. Finally, we can make indirect observations of magmatic processes by studying the products of volcanic eruptions, which provide snapshots of the magmatic system at the time of eruption, to try to unravel the architecture and evolution of magmatic systems (Wallace et al. 1999; Cooper et al. 2012; Gualda and Ghiorso 2013a; Tavazzani et al. 2020; Black and Andrews 2020; Gualda et al. 2022).

The key benefits of this approach are that it emphasizes natural systems, and it allows the investigation of ancient systems that are inaccessible for direct observation.

Silicic volcanic systems have led to some of the most devastating eruptions on record, reaching volumes of hundreds to thousands of cubic kilometers (Lowenstern et al. 2006; Self 2006; Miller and Wark 2008; Bryan et al. 2010) erupted over relatively short periods (days to months, up to decades (e.g., Wilson and Hildreth 1997; Wilson 2001; Hasegawa et al. 2024; Gravley et al. 2025). It is increasingly recognized that the bodies of magma that feed such eruptions are ephemeral features of the crust (Gualda et al. 2012; Matthews et al. 2012; Cooper and Kent 2014; Till et al. 2015; Pamukçu et al. 2015a; Gualda and Sutton 2016; Shamloo and Till 2019; Lubbers et al. 2022; Pitcher et al. 2026). The absence of eruptions with magnitude greater than VEI 6 (VEI: Volcanic Explosivity Index; Newhall and Self 1982) in the 20th and 21st centuries, which could be directly observed by modern methods, emphasizes the importance of inferences drawn from the deposits formed from eruptions of this magnitude. Importantly, we have very limited information on the configuration of volcanic plumbing systems in the moments leading to VEI 6+ caldera-forming eruptions. In this sense, the study of ancient systems is critical to better understand the pre-eruptive architecture of magmatic systems that feed such eruption.

In this study, our goal is to assess the depths and thicknesses of silicic magma bodies that feed VEI 6+ eruptions. We take a novel approach to this problem, using the range of pressures retrieved from rhyolite-MELTS geobarometry using matrix glass compositions (see also Black and Andrews 2020). Our data consist of a compilation of matrix glass compositions and associated geobarometry results from a suite of deposits of high-silica rhyolite eruptions that we have studied in detail over the last 15 years (Gualda et al. 2018, 2022; Pamukçu et al. 2020, 2021; Pitcher et al. 2021, 2026; Smithies et al. 2023; Harmon et al. 2024a, b). This compilation includes data from the Bishop Tuff (Long Valley, USA); three volcanic systems in Central Hokkaido, Japan; the Aira Volcanic Center in Kyushu, Japan; and several volcanic systems in the Taupō Volcanic Zone (TVZ), New Zealand. Importantly, though our dataset is not comprehensive, it includes some of the largest Quaternary eruptions known from the geological record, and it encompasses systems from varied geological settings and tectonic regimes. We focus primarily on the depths and thicknesses of magma bodies that fed volcanic eruptions with total erupted volumes of 10s to 1000s of cubic kilometers (VEI 6 or larger), and we seek general patterns in the distribution of melt-dominated magmas within the crust in the moments leading to VEI 6+ eruptions, with implications for the growth of these magma bodies prior to storage and eruption.

2. Dataset and methods

The dataset used in this study is compiled from several prior studies of different volcanic systems worldwide (in order of first publication):

1. Chimp, Kaingaroa, and Ohakuri Ignimbrites, TVZ Flare-Up, TVZ, New Zealand (Gualda et al. 2018; Smithies et al. 2023)
2. Taupō and Oruanui Ignimbrites, Taupō Volcanic Center, TVZ, New Zealand (Pamukçu et al. 2020, 2021)
3. Tokachi, Tokachi-Mitsumata, and Biei Ignimbrites, Central Hokkaido, Japan (Pitcher et al. 2021)

4. Bishop Tuff, Long Valley, USA (Gualda et al. 2022)
5. Whakamaru Group Ignimbrites, TVZ, New Zealand (Harmon et al. 2024a, b)
6. AT Eruption, Aira Caldera, Kyushu, Japan (Pitcher et al. 2026)

The dataset includes data for 391 individual pumice clasts for which we have determined matrix glass major-element compositions, and it also includes pre-eruptive storage pressures determined using the rhyolite-MELTS geobarometer (Gualda and Ghiorso 2014), as calculated from the matrix-glass compositions in the original studies.

One important advantage of our dataset is that all the compositional data were collected with the same instrument (i.e., an energy-dispersive spectrometry system attached to a scanning electron microscope; hereafter SEM-EDS) using the same techniques and analytical protocols, which have been shown to yield data of excellent quality for silicic glasses (Gualda et al. revised). This facilitates comparison of compositional data. Further, calculations of pre-eruptive storage pressures were performed using the same method – rhyolite-MELTS geobarometry (Gualda and Ghiorso 2014) – which has been demonstrated to yield accurate and precise results for high-silica rhyolites saturated in quartz and feldspars (Bégué et al. 2014b; Pamukçu et al. 2015b; Gualda et al. 2019a; Pitcher et al. 2021; Smithies et al. 2023).

2.1. Overview of analytical methods

All analytical data presented here were collected in the Department of Earth & Environmental Sciences at Vanderbilt University using a Tescan Vega3 Variable-Pressure Scanning Electron Microscope (SEM) with an attached Oxford AZtecEnergy Advanced Microanalysis System equipped with an X-Max 50 mm^2 large-area Silicon Drift Detector (SDD) Energy Dispersive Spectrometer (EDS).

All data were collected using the same analytical protocol: 15 kV incident beam, beam current in the 2-5 nA range (the SEM does not have direct beam current control; rather, we select a beam intensity that yields currents in the desired range), and 15 mm working distance (as optimized for our instrument). EDS spectra live acquisition times are 15 s, using rectangular or irregular acquisition areas (depending on the vesicle textures of each pumice clast) to help minimize Na migration. We set the SDD process time to 4, which yields a good compromise between spectral resolution and count rate in the detector. Pulse pileup and ZAF corrections are applied during quantification, which is performed using the Oxford software AZtec using factory standard measurements, with oxygen calculated by stoichiometry, and results normalized on an anhydrous basis.

For each pumice clast, compositions for a total of 10-20 individual acquisition areas free of vesicles or crystals are obtained. Before further data processing, we identify outlier compositions using the interquartile range (IQR; outlier values are outside the range of median±1.5*IQR), which usually result from accidental analysis of parts of crystals or vesicles. The best estimate of the pumice glass composition is obtained by averaging the non-outlier values for each oxide; the standard deviation of glass compositions for each pumice clast thus includes both the effects of analytical uncertainty and natural variability within the analyzed glass. Quality control is performed during each analytical session by measuring the composition of USGS reference material RGM-1 (Flanagan 1976; Gladney and Roelandts 1988), which was fused into glass at Vanderbilt University. For further details, the reader is referred to the individual studies and Gualda et al. (revised). In particular, Gualda et al. (revised) present a large compilation of analyses of the RGM-1 standard obtained over almost 15 years, which show excellent precision and accuracy over time.

2.2. Overview of pre-eruptive storage pressure calculations using rhyolite-MELTS

Major-element matrix glass compositions are used as input into the rhyolite-MELTS geobarometer, which we use for the calculation of what we refer to as pre-eruptive storage pressures (Gualda and Ghiorso 2014; Gualda et al. 2019b). The premise of the method is that the matrix glass from pumice clasts records the major-element composition of melt that equilibrated with the crystal assemblage observed in the studied pumice clasts. We focus on units that erupted explosively under the assumption that equilibration of major-element compositions during eruptive ascent is minimal. Importantly, the individual studies from which our data are compiled do not find evidence for significant syn-eruptive equilibration of melt compositions.

For this study, we limit ourselves to pumice clasts in which quartz and at least one type of feldspar are observed (Table 1). Many of the systems studied are devoid of sanidine (Oruanui and Taupō Ignimbrites of the Taupō Volcanic Center; most ignimbrites of the TVZ flare-up; AT Eruption deposits), with only plagioclase and quartz as felsic minerals in the crystallizing assemblage. Other systems are characterized by the presence of sanidine in all samples (Bishop Tuff and Biei Ignimbrite). Finally, some of the systems have both sanidine-bearing and sanidine-absent pumice clasts (Whakamaru Group Ignimbrites, Tokachi Ignimbrite, and Tokachi-Mitsumata Ignimbrite). The systems studied here are composed primarily by quartz-bearing pumice, with rare or no quartz-free pumice. In the case of the Taupō Ignimbrite, quartz is observed in only minor abundance, but Pamukçu et al. (2020, 2021) demonstrate that glass compositions show evidence of saturation in quartz. Hence, we do not expect that our focus on quartz-feldspar assemblages will significantly bias our results and interpretations.

We thus follow the method of Gualda & Ghiorso (2014) to calculate, as appropriate for each pumice clast, pressures with quartz-1 feldspar (Q1F) in the sanidine-absent cases or quartz-2 feldspar (Q2F) in the sanidine-bearing cases. In both cases, rhyolite-MELTS calculations are used to determine the saturation temperatures of quartz and feldspars as a function of pressure. Because the composition used for each rhyolite-MELTS calculation is the matrix-glass composition, and crystallization of any solid phase would lead to a change in melt composition, we seek conditions along the liquidus under which the observed felsic phases are simultaneously in equilibrium with a melt of the given composition (Figure 1). We thus look for a 2-phase (in the case of Q1F pressures) or 3-phase (in the case of Q2F pressures) intersection between the saturation surfaces calculated by rhyolite-MELTS v. 1.0 for each glass composition. In practice, we use a P-T grid for the rhyolite-MELTS calculations, with typical temperature and pressure intervals of 1 °C and 25 MPa, respectively. In order to calculate the best intersection, we use a parabola-fitting procedure described in detail in Gualda & Ghiorso (2014).

By focusing on the felsic assemblage of quartz-bearing pumice, we leverage the fact that the stability of quartz and feldspars is independent of oxygen fugacity, a parameter that is notoriously difficult to properly constrain and makes pressure calculations with mafic minerals and Fe-Ti oxides more difficult and potentially less precise (Harmon et al. 2018; Smithies et al. 2025). Since we do not need accurate information on the oxygen fugacity, we reduce the number of assumptions necessary in our calculations and generally simplify determination of pre-eruptive storage pressures.

We have not determined H_2O-CO_2 contents in melt inclusions for samples in this study (with the exception of AT Eruption deposits), but H_2O-CO_2 values present in the literature (Wallace et al. 1999; Anderson et al. 2000; Liu et al. 2006; Bégué et al. 2014b; Myers et al. 2019; Pitcher et al. 2026) invariably indicate high H_2O concentrations consistent with high H_2O activity during crystallization of the felsic minerals. Gualda & Ghiorso (2014) and Ghiorso & Gualda (2015) demonstrate that, for conditions of high H_2O activity (i.e., near or at fluid saturation), quartz-feldspar pressures are not particularly sensitive to H_2O activity. This can be explained by the fact that the effect of pressure on the saturation temperature is similar for quartz and feldspars, such that the position of the intersection between the saturation surfaces as a function of pressure is unchanged as a function of H_2O activity, for high H_2O activity values. This is consistent with experimental evidence in the haplogranitic system (Tuttle and Bowen 1958; Johannes and Holtz 1996; Blundy and Cashman 2001), which shows that the position of the quartz-feldspar cotectic as a function of pressure is relatively insensitive to H_2O activity. At the same time, these studies suggest that crystallization temperatures cannot be retrieved using rhyolite-MELTS without appropriate estimates of H_2O activity (see Pamukçu et al. 2015b; Pitcher et al. 2021 for more detailed discussions and comparisons between geothermometers), because liquidus temperatures are a strong function of H_2O activity (e.g., Johannes and Holtz 1996) – for this reason, we do not attempt to estimate temperatures using the rhyolite-MELTS results, and we choose to focus on the information that can be gathered from pressure estimates.

It is important to consider uncertainties associated with pressure estimates derived using the rhyolite-MELTS geobarometer. Bégué et al. (2014b), Pamukçu et al. (2015b), and Gualda et al. (2019a) compare rhyolite-MELTS pressures with independently constrained pressures determined using H_2O-CO_2 in melt inclusions and Al-in-hornblende geobarometry. The comparisons show that rhyolite-MELTS pressures agree with independent estimates within error of the determinations. Pitcher et al. (2026) show that H_2O-CO_2 saturation pressures overlap significantly with rhyolite-MELTS pressures, with very good agreement between the shallowest H_2O-CO_2 pressures and the rhyolite-MELTS pressures. Further, in several of the studies compiled here (e.g., Pamukçu et al. 2020, 2021; Gualda et al. 2022), rhyolite-MELTS pressures are compared with expectations based on projection of the matrix-glass compositions onto the haplogranitic ternary using the projection scheme of Blundy & Cashman (2001). We find very good agreement between rhyolite-MELTS pressures and their position relative to relevant quartz-feldspar cotectic curves in the haplogranitic ternary. We thus find no evidence for systematic errors or biases in rhyolite-MELTS quartz-feldspar pressures when compared to independent estimates. Further confirmation of this is given by pressure estimates derived for the Krafla IDDP-1 magma body (Harmon et al. 2025), which show excellent agreement between rhyolite-MELTS pressures and the depth at which the magma body was intersected during drilling.

Given that we focus on differences in pressure within a dataset collected using the same instrumentation and protocols, and using the same thermodynamic calculation procedures, relative uncertainties are more important than absolute errors. Gualda & Ghiorso (2014) employ a Monte Carlo procedure to estimate the precision of the rhyolite-MELTS geobarometer due to the analytical uncertainty associated with the measured glass compositions, and obtain uncertainties of 25 MPa for Q2F pressures and 50 MPa for Q1F pressures (1-sigma). However, Gualda & Ghiorso (2014) use a dataset of compositions from the literature (Wallace et al. 1999; Anderson et al. 2000), which is characterized by relatively large errors in Na_2O concentrations that lead to large uncertainties in the pressure calculations. Further, Gualda & Ghiorso (2014) demonstrate that SiO_2 uncertainties also significantly impact pressure calculations, which is understandable given that quartz-feldspar pressures are a strong function of SiO_2 concentrations (Blundy and Cashman 2001; Gualda and Ghiorso 2013b).

In contrast, all the studies compiled here use the same instrument, and they employ analytical protocols devised to minimize Na migration and to obtain precise SiO_2 concentrations during analysis (for details, see Gualda et al. revised). Estimates of uncertainties on these data obtained using a Monte Carlo approach initially employed by Gualda & Ghiorso (2014) are presented in several of the original studies and show similar results (all values are reported at the 1-sigma level in this work):

- 38 MPa for Q1F and 24 MPa for Q2F, Biei Ignimbrite, Central Hokkaido, Japan (Pitcher et al. 2021)
- 8-21 MPa for Q1F for Taupō Ignimbrite, TVZ, New Zealand (Pamukçu et al. 2021)
- 9 MPa for Q1F for Chimp Ignimbrite, 21 MPa for Q1F for Kaingaroa Ignimbrite, and 13 MPa for Q2F for Whakamaru Group Ignimbrites, TVZ, New Zealand (Smithies et al. 2023)

While Gualda & Ghiorso (2014) suggest that uncertainties associated with Q1F pressures should be higher than those associated with Q2F pressures – and that expectation is borne out in the results of Pitcher et al. (2021) – results from Pamukçu et al. (2021) and Smithies et al. (2023) show that Q1F pressures can have low uncertainties (~10 MPa) in cases in which the glass is particularly homogeneous. Such low uncertainties are particularly achievable when pressures are greater than ~150 MPa because the slopes of the saturation temperature surfaces become progressively more distinct with increasing pressure.

We complement the set of uncertainty estimates discussed above with similar determinations for the Bishop Tuff dataset (Gualda et al. 2022). We use the same Monte Carlo approach used in previous studies and follow the procedure of Pamukçu et al. (2021) by using 200 synthetic compositions derived using the mean and standard deviation from the group of 10-20 analysis obtained using the SEM-EDS. We apply the approach to three pumice clasts representative of each compositional group of the Bishop Tuff (see section 3.2; i.e., F5-507 from the early-erupted deposits; F9-954 from the eastern late-erupted deposits; and AB-6203 from the northern late-erupted deposits). We obtain uncertainties in the range of 23-28 MPa for Q2F pressures.

Overall, based on the published studies cited above, we conclude that uncertainties on the order of 20-25 MPa are most characteristic for pressures determined using the rhyolite-MELTS geobarometer with glass data collected at Vanderbilt, with a possible range of 10-40 MPa.

2.3. Statistical treatment of compiled data

One of the primary goals of the present study is to investigate the extent to which we can constrain the thickness of the magma bodies that feed VEI 6+ eruptions using pressure data obtained using the rhyolite-MELTS geobarometer. An important consideration, then, is how the dispersion in the dataset from each volcanic system studied compares with the pressure uncertainties discussed above. We use the mean square weighted deviation (MSWD; Wendt and Carl 1991) to identify under and overdispersion within our dataset.

When the MSWD is between $1 - \sqrt{2/(n-1)}$ and $1 + \sqrt{2/(n-1)}$, where n is the number of pressure values in any given population of pressures, the distribution is considered underdispersed (Klein and Eddy 2024), and the variation in pressure values can be entirely explained by the uncertainties associated with each pressure value. This is consistent with a single pressure population, with variability mostly imprinted from analytical uncertainty rather than variability due to several pressure populations. In these cases, the pressure distribution we measure provides a maximum potential pressure variation, and we use equation 9 of Klein & Eddy (2024) to constrain the maximum thickness of the magma body represented by the population of pressure estimates:

$$\Delta h^{MAX} = \frac{\sigma}{3.34 - 3.39n^{-0.027}}$$

where Δh^{MAX} is a maximum bound on the thickness of the magma body, σ is the uncertainty associated with the pressure calculations (as derived using our Monte Carlo procedure), and n is the number of pressures in the population. In most cases in this study, we use the same uncertainty for all pressure estimates in a population, which is also the value we use for σ. In the case of the Tokachi Ignimbrite and the Tokachi-Mitsumata Ignimbrite, Q1F pressures have a different uncertainty from Q2F pressures; we thus follow the approach of Klein & Eddy (2024) and calculate a weighted average uncertainty value, which we use for σ.

In the cases in which the MSWD is larger than $1 + \sqrt{2/(n-1)}$, the data is considered overdispersed; in these cases, the variability in pressure values is larger than what can be explained by the individual uncertainties associated with each pressure. It follows that a minimum thickness can be constrained using equations 7 and 8 of Klein and Eddy (2024). However, none of our datasets are overdispersed, so we do not consider this further.

Finally, MSWD values lower than $1 - \sqrt{2/(n-1)}$ are typically interpreted to indicate that uncertainties have been overestimated (Klein and Eddy 2024). Interestingly, we argue that this result can – in some cases – help identify cases in which uncertainties calculated using our Monte Carlo procedure may be overestimated.

Given that the approach above carries significant assumptions and caveats, we also use the dispersion in each population to estimate magma body thicknesses. We use three similar methods to quantify dispersion from a population of pressures to constrain magma body thickness, which we hereafter refer as calculated magma thickness:

1. We select the 95% confidence interval from the observed population, by excluding the lowermost (0%-2.5%) and uppermost (97.5%-100%) pressure values. A weakness of this approach is that it implicitly assumes that outliers are symmetrically distributed, which is not necessarily the case. We denote this quantity as “95% CI” in figures.
2. We remove outlier pressure values using the IQR of each population of calculated pressures – any values outside the range of median ± 1.5 IQR are typically considered outliers – and we calculate the thickness represented by each population as the difference between the maximum and minimum pressures after exclusion of outlier

values (i.e., maximum value minus minimum value with outliers excluded). The main disadvantage of this procedure is that it is very sensitive to the identification of outlier values. We denote this quantity as “Max-Min [OE]” in figures.

3. Given that non-outlier values are typically within ±1.5*IQR, a third estimate of thickness is given by the value of 3*IQR. The main weakness of this metric is that it may overestimate the thickness in cases in which there are no outliers; thus, the bounds of 3*IQR are greater than the difference between the minimum and maximum. We denote this quantity as “3*IQR” in figures.

We convert pressures into depths by assuming a crustal density of $2.7 * 10^3$ kg/m^3, which leads to a conversion factor of 0.037 km/MPa, such that, for instance, 100 MPa corresponds to a calculated depth of 3.7 km.

We compare the thicknesses calculated using the geobarometric methods above to estimates of thickness that can be derived from the geological evidence for known erupted volumes and caldera footprint areas (see Black and Andrews 2020), in which case the magma body thickness is simply the erupted volume divided by the caldera area (denoted in figures as “Vol/Area”). We expect that the magma body thicknesses derived in this way will carry substantial uncertainties. Further, there are questions on how to interpret caldera footprint areas in the context of eruptions that may have been fed by multiple magma bodies (e.g., Gualda et al. 2022). Nonetheless, comparisons of thicknesses calculated using geobarometry and those obtained from volume:area values serve as an important check as to whether magma body thicknesses calculated from pressure estimates are consistent with available geological evidence from each deposit.

3. Results

3.1. General characteristics of the matrix-glass compositions

All the matrix-glass compositions in our compilation are rhyolites with SiO_2 > 75.0 wt.% (Figure 2). The Taupō and Chimp Ignimbrites have lower SiO_2 (<76.0 wt.%) and higher FeO (>1.5 wt.%) than the rest of the dataset; they also have generally high CaO and low K_2O. Further, they yield the highest pressures (285-345 MPa).

Aside from the Taupō and Chimp Ignimbrites, the matrix-glass compositions are all high-silica rhyolite with SiO_2 between 76.5 and 78.3 wt.%. The concentrations of CaO and FeO separate the high-silica rhyolite compositions into several groups. Units that are characterized exclusively by an assemblage of quartz and plagioclase (Q1F: Oruanui, Kaingaroa, and Ohakuri Ignimbrites in the TVZ and the AT Eruption in Kyushu, Japan) have K_2O < 4.3 wt.%, while units characterized exclusively by quartz and 2 feldspars (Q2F: Bishop Tuff in the US and Biei in Central Hokkaido) and units in which Q1F and Q2F assemblages coexist (Tokachi and Tokachi-Mitsumata in Central Hokkaido; Whakamaru in the TVZ) have K_2O > 4.3 wt.%. In the case of coexisting Q1F and Q2F assemblages, higher CaO values are typical of Q1F compositions relative to Q2F compositions. Pressures for the high-silica rhyolites span the range of 50 to 200 MPa (1.9-7.4 km).

3.2. Bishop Tuff

The Bishop Tuff (Sheridan 1965; Bailey et al. 1976; Hildreth 1979) is the focus of the detailed study by Gualda et al. (2022), in which a total of 221 pumice clasts were studied, with 143 of them yielding Q2F pressure estimates. Gualda et al. (2022) divide the Bishop Tuff deposits into three groups, distinguished based on their stratigraphic position and matrix-glass compositions: (1) early-erupted deposits (EBT), which appear exclusively in the eastern and southern sector of the deposits; (2) late-erupted deposits that overlie EBT deposits in the eastern and southern sector of the deposits (LBT-East); (3) late-erupted deposits that appear to the north of the caldera (LBT-North). While the stratigraphic relationship between EBT and LBT-East is straightforward, with LBT-East overlying EBT in locations where they coexist, LBT-North is separated from EBT and LBT-East by the older Glass Mountain volcanic edifice and by the Long Valley Caldera, such that contact relations between the two sectors are unknown (Wilson and Hildreth 1997). Nonetheless, since both LBT-East and LBT-North are characterized by pyroxene-bearing pumice, and EBT pumice is pyroxene-free, it is generally assumed that LBT-East and LBT-North erupted simultaneously (Hildreth 1979; Hildreth and Wilson 2007). This is also consistent with inferred vent locations based on the distribution of lithic clasts in the deposits (Hildreth and Mahood 1986; Wilson and Hildreth 1997). Available Q2F pressure estimates from Gualda et al. (2022) include 75 pressures for EBT, 50 for LBT-East, and 18 for LBT-North.

Results for the Bishop Tuff are shown in Figure 3, Figure 4, and Table 2. Overall, as originally observed by Gualda et al. (2022), the pressure ranges and distributions show significant overlap between all units (EBT, LBT-East, and LBT-North), with LBT-North showing slightly lower median pressures (133 MPa for EBT, 135 MPa for LBT-East, 115 MPa for LBT-North; see Figure 3a-b). Geobarometric thicknesses (i.e., those calculated using the 95% CI, IQR*3, and Max-Min [OE] methods) are similar to each other, ranging between 1.1 and 2.6 km (see Figure 4). Assuming uncertainties of 25 MPa (as calculated using our Monte Carlo procedure), the maximum bound on the thickness (labeled "Δh_MAX") is similar to the calculated thicknesses for EBT and somewhat larger than those for LBT-East and LBT-North; the trend of increasing maximum thickness (i.e., Δh_MAX) from EBT to LBT-East to LBT-North is due to the different number of pressure estimates for each unit, and does not necessarily imply significant differences in thicknesses between the inferred magma bodies. Interestingly, calculated MSWD values for each compositional subgroup are smaller than the expected lower thresholds (see Table 2), suggesting that our estimated uncertainties for the Bishop Tuff might be overestimated. For comparison, we also show MSWD and maximum thickness values for an uncertainty of 20 MPa, which reveals MSWD values that fall in between lower and upper MSWD thresholds, and maximum thicknesses that are closer to the calculated thicknesses.

In order to compare the thickness calculated from the rhyolite-MELTS pressures with that suggested by the volume:area value (see Table 1), we combine all pressures and treat them as a single population (Figure 3b). This seems warranted given the similarities in pressure distribution between the three compositional groups of Gualda et al. (2022)(see Figure 3a). Our results suggest that magmas were present at a single horizon centered around 135 MPa (~5 km) and vertically spanning ~2.5 km, consistent with the geological evidence given by the volume:area value of 3.0 km. Similarly to the individual compositional groups, when all Bishop Tuff results are combined, the MSWD value is lower than the minimum threshold calculated with uncertainties of 25 MPa, while the MSWD value for uncertainties of 20 MPa falls between the minimum and maximum thresholds (Table 2). Regardless of the choice of uncertainty, the low MSWD values confirm that the data can be considered a single pressure population.

3.3. Whakamaru Group Ignimbrites

The Whakamaru Group Ignimbrites (Brown et al. 1998) include some of the largest eruptions in the TVZ, and they are the focus of detailed studies of both the ignimbrite and pyroclastic fall records by Harmon et al. (2024a, b). Harmon et al. (2024a, b) follow the compositional grouping defined by Brown et al. (1998) and divide 83 individual pumice clasts into four types (labeled A-D) based on compositional characteristics. While types A, B, and C are readily differentiated from one another by matrix glass major and trace-element compositions, type D can only be distinguished from type A using whole-rock data, which could not be obtained for the small pumice lapilli of the pyroclastic fall material studied by Harmon et al. (2024a); however, Harmon et al. (2024b) present whole-rock compositions for pumice clasts from the ignimbrite deposits, which resulted in only one out of 42 pumice clasts classified as type D. Similarly, Brown et al. (1998) argue that type D is significantly less abundant than types A-C. Given that the pyroclastic fall pumice clasts classified as type A by Harmon et al. (2024a) may include a small number of type D pumice clasts, but no substantial differences in storage pressures were observed by Harmon et al. (2024a, b) between types A and D, we combine the single type D pumice clast from the ignimbrites studied by Harmon et al. (2024b) and any misidentified type D pumice clasts from the pyroclastic fall material with type A. Given the small fraction of pumice and magma represented by type D pumice, this choice does not change our interpretations.

The rhyolite-MELTS pressure results for the three compositional types yield similar and overlapping pressures (Figure 5a), with median values between 95 and 100 MPa (3.5-3.7 km) and calculated thicknesses of 2.3-3.8 km (Figure 4 and Table 2. The MSWD values obtained for the three types are all between the minimum and maximum threshold values. Treated as individual populations, the maximum thicknesses (Δh^{MAX}) obtained for the three compositional types are between 3.4 and 4.4 km (Figure 4 and Table 2).

Similarly to the case of the Bishop Tuff, we combine the results for all compositional types (Figure 5b) in order to compare the thickness derived from geobarometry with the ratio of geological estimates (from Miller et al. 2026) of erupted volume (1,500 km^3) and caldera area (900 km^2; see Table 1). Also, similarly to the case of the Bishop Tuff, combining the data into a single population is justified by the fact that all three compositional types show overlapping pressure distributions. The MSWD value for the combined dataset is within the minimum and maximum threshold values, such that our data are consistent with magmas occupying a horizon of 2.6-3.5 km thickness (Figure 4 and Figure 5).

3.4. Taupō Volcanic Center

The Taupō Volcanic Center is the locus of the most recent supereruption on Earth – the ~25 ka, 530 km^3 Oruanui Ignimbrite (Wilson 2001; Wilson et al. 2006) – and is also the site of one of the most recent VEI 6 eruptions on Earth – the ~1.8 ka, 35 km^3 Taupō Ignimbrite (Wilson 1993; Hogg et al. 2019). The Oruanui and Taupō eruptions are the focus of Pamukçu et al. (2020), and the relevant pressure estimates are summarized in Figure 4 and Figure 6a. In our compilation, we present only matrix glass data, and we exclude pressures determined using glass inclusions.

As discussed in detail by Pamukçu et al. (2020, 2021), data for the Oruanui system is consistent with eruption of magmas located in the shallow crust, and we obtain a median pressure of 140 MPa (~5.2 km), with calculated magma body thicknesses between 1.8 and 2.3 km (Figure 4 and

Table 2). The MSWD value is consistent with magmas being present in a single crustal horizon. Because the number of compositions yielding pressure determinations is relatively small (n = 18), the maximum thickness (Δh^{MAX}) is calculated to be relatively large (I.e., 3.6 km). Using the erupted volume and caldera area listed in Table 1, we obtain a volume:area value of 3.9 km.

For the Taupō system, also following Pamukçu et al. (2020, 2021), we infer a much deeper (median of 330 MPa; ~12.2 km) magma body, with a calculated thickness of 1.1-1.3 km; the MSWD value indicates a single pressure population, with a maximum thickness of 2.7 km (Figure 4 and Table 2). While the maximum thickness (Δh^{MAX}) is more than double the inferred thickness, we emphasize that the dataset includes only eight datapoints, which leads to a large maximum thickness estimate.

3.5. TVZ Flare-Up Ignimbrites

The TVZ Flare-Up (Gravley et al. 2016) was a period in which copious volcanism in the Central TVZ led to – in addition to the Whakamaru Group Ignimbrites – at least six caldera-forming eruptions with a total magmatic volume at least 1,000 km^3 over a timespan of <100 ka (~320-240 ka; Smithies et al. 2023). Ignimbrites of the TVZ Flare-Up were the focus of studies by Gualda et al. (2018) and Smithies et al. (2023). Here we focus on three eruptions from these studies that show variable results, as summarized in Figure 4 and Figure 6b.

The Chimp Ignimbrite (50 km^3 DRE; see Table 1), which originated from the Kapenga Caldera, was one of the first ignimbrite eruptions in the TVZ flare-up. It is characterized by relatively deep (290 MPa, 10.7 km) calculated pressures (Gualda et al. 2018; Smithies et al. 2023). There is a very tight distribution of pressures for the Chimp-A compositional group, resulting in calculated thicknesses between 0.1 and 0.3 km (Figure 4, Figure 6b, Table 2), in excellent agreement with the volume:area value of 0.2 km (Table 1). We note that at least four caldera collapse events have been attributed to the Kapenga Caldera (Wilson et al. 2009), thus this area is a maximum for the Chimp eruption and the resulting volume:area value is a minimum estimate. The MSWD value is low but within the range given by the lower and upper MSWD thresholds (Table 2). The maximum expected thickness (Δh^{MAX}) is much larger than the calculated thicknesses, despite the small uncertainties – this is a result of the low number of pressures for this unit (i.e., n = 9). Our dataset includes an additional 5 compositions that correspond to other compositional groups from the Chimp Ignimbrite, and which give distinctively shallower pressures (e.g., ranging between 170 and 260 MPa). These data points are not included in Figure 6b because they do not belong to the tightly clustered population representative of the Chimp-A compositional type – these data points suggest that other crustal levels may also have contributed to the eruption (see Smithies et al. 2023). Nonetheless, our data show that a significant volume of magma was located at relatively deep crustal levels, and it could explain the bulk of the volume of the eruption.

The Kaingaroa Ignimbrite (100 km^3 DRE) is a younger unit of the TVZ Flare-Up, and it also reveals a tight distribution of pressures, but at shallower crustal levels (160 MPa, 5.9 km), with calculated thickness of 0.6-1.0 km (Figure 4, Figure 6b, Table 2), in excellent agreement with the volume:area value of 1.0 (see Table 1). The MSWD value is low but within the lower and upper threshold values. Similarly to the case of the Chimp Ignimbrite (and also the Taupō Ignimbrite), the relatively large maximum expected thickness (Δh^{MAX}) is substantially higher than the calculated thicknesses due to the low number of pressures (n = 11).

Finally, data for the Ohakuri Ignimbrite (50 km^3 DRE) reveal magmas at a shallower crustal level (100 MPa, 3.7 km), with calculated thicknesses of 1.3-2.8 km (Figure 4, Figure 6b, Table 2). The MSWD value is within the lower and upper threshold values, and the maximum bound thickness (Δh^{MAX}) is 4.1 km. The volume:area value of 2.0 km (Table 1) suggests magma distribution over a thickness smaller than the calculated thicknesses. We did not include data from the Ohakuri Fall deposits, which have been inferred to represent a different batch of magma emplaced outside of the Ohakuri Caldera (Bégué et al. 2014a).

3.6. Central Hokkaido Ignimbrites

The Island of Hokkaido (northern Japan) is a volcanically active area with abundant caldera-forming volcanism since the Pleistocene (Ikeda and Mukoyama 1983; Ikeda 1991). Pitcher et al. (2021) focus on three main Quaternary ignimbrites from Central Hokkaido: Biei (BIEI), Tokachi (TOKA), and Tokachi-Mitsumata (TOKM) Ignimbrites. The Biei Ignimbrite is composed of a single pumice compositional type, which is characterized by the presence of quartz and two feldspars. In contrast, both the Tokachi and Tokachi-Mitsumata Ignimbrites have two pumice types, distinguished by major and trace-element compositions, as well as by the fact that types 1F of Pitcher et al. (2021) are characterized by quartz and plagioclase with no sanidine, while types 2F are characterized by quartz and two feldspars.

As originally demonstrated by Pitcher et al. (2021), despite the presence of different compositional groups in the Tokachi and Tokachi-Mitsumata Ignimbrites, both types 1F and 2F yield overlapping pressures, which are also similar to those for the Biei Ignimbrite. Results for all three ignimbrites are summarized in Figure 4, Figure 7a, and Table 2. All three ignimbrites yield median pressures of ~110-130 MPa (4.1-4.8 km), and 95% CI thicknesses of 1.7-2.0 km. The IQR*3 thicknesses are quite a bit more variable, with the more dispersed distribution for the Tokachi Ignimbrite leading to a thickness of 4.1 km and the tighter distribution for the Tokachi-Mitsumata Ignimbrite yielding a thickness of 0.9 km. The Max-Min [OE] pressures are more tightly distributed, giving a range between 0.6 and 2.0 km. Pitcher et al. (2021) calculate uncertainties of 25 MPa for Q2F pressures and 40 MPa for Q1F pressures, which we use in our treatment. As a result, average uncertainties for the Tokachi and Tokachi-Mitsumata Ignimbrites depend on the number of Q1F and Q2F pressures in each eruption; we calculate average uncertainties (weighted by the number of pumice clasts with one or two feldspars) of 28 MPa for the Tokachi Ignimbrite and 35 MPa for the Tokachi-Mitsumata Ignimbrite. The MSWD values for all three ignimbrites are between the lower and upper thresholds. Because the uncertainties estimated by Pitcher et al. (2021) are larger than in the other datasets included in this study, the maximum bound on magma thicknesses (Δh^{MAX}) are also large, between 5.1 and 7.6 km. The volume:area values are 2.0 km for Tokachi and 0.9 km for Tokachi-Mitsumata. The caldera size of Biei is not well constrained, so we are unable to calculate a volume:area value for this eruption.

3.7. AT Eruption

The 30 ka Ito Ignimbrite (Nagaoka et al. 2001; Smith et al. 2013; Geshi et al. 2020) is the largest eruptive unit of the Aira Caldera in the Island of Kyushu in southern Japan, and it is the focus of a detailed study by Pitcher et al. (2026). Ignimbrite deposition was preceded by deposition of an important pyroclastic fall unit, the Osumi Fall. Since both units are inferred to have been formed from the same eruptive event, we treat them in combination here – collectively, the 400 km^3 caldera-forming eruption is referred to as the AT Eruption. The Osumi Fall unit includes grey pumice, which is not quartz-saturated – it is thus unsuitable for the analysis performed here. Importantly, the grey pumice is a volumetrically minor constituent of the erupted magma, and it is isotopically distinct from the volumetrically dominant white pumice (Kuritani 2023; Nishihara et al. 2024). We thus exclude results from grey pumice, but such exclusion should not affect the conclusions drawn here. Results suggest a single magma body at a median pressure of 115 MPa (4.3 km) and calculated thickness between 2.5 and 3.7 km (Figure 4, Figure 7b, Table 2). The MSWD values are within the lower and upper thresholds, and the maximum bound on thickness (Δh^{MAX}) is 3.1 km, generally in agreement with the calculated thicknesses. The volume:area value is 2.0 km (Table 1).

4. Discussion

4.1. Depths of magmas feeding VEI 6+ silicic eruptions

We summarize the results presented above in Figure 4 and Figure 8. Inspection of these figures reveals that most magmas associated with VEI 6+ silicic eruptions are stored at a range of depths from ~2 to 7 km, with median depths of 3.0-5.1 km. This suggests that the magma bodies that feed VEI 6+ eruptions are primarily stored at similar crustal levels in the shallow crust. This does not preclude deeper crustal levels from being important locations of magma reservoirs; however, if such reservoirs exist, they are not typically mobilized during large-scale eruptions like those investigated here.

Comparison of median depth with volume (Figure 9) shows that, for magma volumes > 50 km^3, there is no correlation between depth and volume. Our results strongly suggest that large volumes of melt-dominated magma were present – likely ephemerally (e.g., Gualda et al. 2012; Matthews et al. 2012; Allan et al. 2013; Cooper and Kent 2014; Pamukçu et al. 2015a; Gualda and Sutton 2016) – in the shallow crust in volcanically active areas. The fact that erupted magmas emanate primarily from the shallow crust is consistent with the idea that the low density of the exsolved fluid phase at shallow crustal levels is an important driver of explosive eruptions (Tramontano et al. 2017; Huber et al. 2019). This is also consistent with the idea that high-silica rhyolites (≥ 76 wt. % SiO_2), such as many of the eruptions detailed here, can only be formed in the shallow crust (< 350 MPa) due to the location of the quartz-feldspar cotectic as a function of depth (see Gualda and Ghiorso 2013b).

Results for two smaller eruptions from the TVZ show that magmas erupted from deeper crustal levels: Chimp-A (50 km^3) at 10.7 km and Taupō (35 km^3) at 12.2 km. This suggests that, under suitable conditions, melt-dominated rhyolitic magmas from deeper levels can reach the surface and feed explosive eruptions. The TVZ is characterized by significant crustal extension (Villamor and Berryman 2001; Spinks et al. 2005; Villamor et al. 2017), which may facilitate eruption to the surface from deeper levels than what is possible in other tectonic environments. Interestingly, the Chimp eruption took place at the early stages of a magmatic cycle during the TVZ flare-up (Gravley et al. 2016; Gualda et al. 2018; Smithies et al. 2023), while the Taupō eruption followed substantial changes in the Taupō Volcanic Center that may hint at the onset of a new magmatic cycle. This may suggest that specific conditions at the early stages of magmatic cycles in the TVZ facilitate eruption of magma from deeper levels.

4.2. Thicknesses of magma bodies feeding VEI 6+ silicic eruptions

We propose three methods to calculate magma thickness using pressures at which matrix-melt compositions were in equilibrium with the observed felsic assemblage in pumice clasts. The results from our analysis are shown in Figure 4b and Figure 8. Thicknesses calculated using the 95% CI, IQR*3, and Max-Min (OE) metrics range from 0.6 to 4.1 km, with a few exceptions. Thicknesses inferred using $\Delta \mathrm{h}^{\mathrm{MAX}}$ are much more variable, but this is a result of the variable number of pumice clasts studied for each of the units and subunits, rather than reflecting real differences in thickness – in this sense, $\Delta \mathrm{h}^{\mathrm{MAX}}$ only provides a maximum bound on the possible thickness. Considering the large volumes involved in these eruptions, we find that the melt-dominated bodies of magma involved in these eruptions had high aspect ratio (diameter/thickness) – from 3 to 23 – indicating oblate shapes that are consistent with the development of calderas at the Earth's surface. Our data further suggest that typical thicknesses for these very large magma bodies are less than ~4 km – a future avenue of research would be to consider what parameters in the magma bodies themselves and in the surrounding crust lead to such relatively homogeneous thicknesses for magma bodies that vary in erupted volume by more than two orders of magnitude.

Importantly, it is usually found that, at shallow crustal depths (~3-12 km), geophysical methods would have difficulty in unambiguously detecting melt-rich magma parcels with thickness similar to or smaller than 1-2 km (e.g., Rasht-Behesht et al. 2020; Maguire et al. 2022; Paulatto et al. 2022). Our data provide direct information on the thicknesses of magma bodies that fed Quaternary VEI 6+ eruptions, and they could help guide the search for thin (<1 km thick) bodies of melt-dominated magma potentially present today. This could have potential implications for hazard assessment in areas of ongoing unrest (e.g., Campi Flegrei, Italy; Santorini, Greece; TVZ, New Zealand).

4.3. Dispersed versus concentrated magmas

Up to this point, the pressure data we have presented have been interpreted to represent the location of melt-dominated magma bodies within the crust. An alternative interpretation is that melt that is dispersed within the crust can be rapidly mobilized to feed eruptions (see, for instance, Cashman and Giordano 2014). In this interpretation, accumulations of large melt-dominated magma may never exist, and eruptions could tap storage regions where melt is dispersed within large volumes of crystal-rich magma mush, as is inferred to be the case in some currently active volcanic areas (e.g., Yellowstone; Huang et al. 2015).

Comparison of the thicknesses derived from geobarometry that we calculate here with volume:area values (Figure 10a) allows us to assess the likelihood of this alternative scenario. We envision three possibilities (Figure 10b):

1. If the estimated thickness agrees with the volume:area value, we infer that erupted magma was concentrated in melt-dominated magma bodies, and these bodies can account for the full volume of erupted material.
2. If the estimated thickness is much larger than the volume:area value, we infer that it is possible that melt was dispersed within crystal-rich magma mush; the larger the difference, the lower the inferred melt concentration within the magma mush.

3. If the estimated thickness is much smaller than the volume:area value, we infer that a melt-dominated magma body existed; however, other crustal levels – not included in analyzed samples – would also have to have contributed to eruption.

In Figure 10a, case 1 is represented by examples that fall along the 1:1 line (labelled "Melt-dominated in Figure 10b). Because of multiple potential sources of uncertainty in both the determination of thickness from geobarometry data and in the volume:area values from geological information, we also show reference lines with deviations from the 1:1 line in increments of 10%, from 7/10:1 to 10/7:1 in Figure 10a. With the data we currently have available, we find that most of the examples studied here fall within a reasonable error envelope of the 1:1 line, consistent with our interpretation that the pressures determined from matrix-glass compositions for these systems reveal the locus of shallow crustal melt-dominated magma bodies that fed eruptions to the surface.

Case 2 is represented by datapoints that fall significantly above the 1:1 line in Figure 10a (labelled "Fully dispersed" and "Hybrid" in Figure 10b). The main candidates for this case include the Taupō Ignimbrite, the deposits of the AT Eruption, and the Whakamaru Group Ignimbrites. We note that the Taupō Ignimbrite yields the deepest pre-eruptive storage pressures of all the deposits studied here. It is also the deposit with the smallest volume (i.e., 35 km^3). As such, it is possible that mobilization of smaller volumes may be easier at deeper crustal levels. It is also worth emphasizing that our dataset only includes eight datapoints for the Taupō Ignimbrite, and further work could significantly improve our understanding of this system. In the case of the AT Eruption, Pitcher et al. (2026) argue that the magma that fed the eruption was mobilized in less than 1,000 years, possibly triggered by the influx of volatiles into the system. This may have made it possible to erupt a large volume of magma (i.e., 400 km^3) from a reservoir that was more dispersed than in other systems. Interestingly, the AT eruption consisted of three phases: the Osumi fall (40 km^3), the Tiramazu fall (10 km^3), and the Ito Ignimbrite (350 km^3), which can be reconciled with extraction of melt from magma mush within eruptive timescales.

Finally, case 3 is represented by datapoints that fall significantly below the 1:1 line in Figure 10a (labelled "Missing magma" in Figure 10b). The Oruanui Ignimbrite is the primary candidate for this case. The dataset we have accumulated for it is relatively small (n = 18), but the eruption has been inferred to have been fed from a complex magmatic system (Allan et al. 2017; Pamukçu et al. 2020). It is therefore understandable that the relatively small sample set used here may not encompass all the variability in the deposit. As such, we cannot discern from our dataset whether the magma system was characterized by a thicker magma body, or if additional data would reveal different magma bodies at other crustal levels. This emphasizes the importance of studying larger numbers of pumice clasts to gain an adequate understanding of the pre-eruptive architecture of magmatic systems.

Overall, we conclude that most VEI 6+ eruptions are fed from melt-dominated magma bodies. This is consistent with the geological evidence given by the usual presence of well-defined caldera structures in the geological record, which are most easily explained by evacuation of shallow bodies of melt-dominated magma in rapid eruption events (e.g., Smith and Bailey 1968; Acocella 2007; Cashman and Giordano 2014; Mullet et al. 2023).

4.4. Growth of supereruption-forming magma bodies

The data compiled here can also be used to explore relationships between estimated thickness and erupted volume. Data in our compilation show that the smallest eruptions (i.e., < 50 km^3) yield thin calculated thicknesses (< 1.5 km), while eruptions with volumes ~100 km^3 show a wider range of thicknesses, possibly as thick as 4 km (Figure 11). In contrast, eruptions with volumes > 200 km^3 all show thicknesses between 2 and 4 km. This may suggest that magma bodies become thicker – at relatively constant aspect ratio – until they reach ~200 km^3. With increasing volume, the thickness remains relatively constant, which suggests that growth takes place by lateral spreading, with a progressive increase in aspect ratio (i.e., magma bodies become progressively more oblate). Future work could investigate the reasons why the thickness of magma bodies that feed the most voluminous eruptions (i.e., VEI 7+) does not seem to surpass ~4 km.

5. Conclusions

In this work, we present a compilation of matrix-glass data and rhyolite-MELTS pre-eruptive storage pressures for several VEI 6+ caldera-forming eruptions worldwide with volumes ranging from 35 to 1,500 km^3, and we assess the thicknesses of the magma bodies that fed these eruptions. Critically, because data in this compilation were collected using the same procedures on the same instrument, we can make meaningful comparisons between these eruptions. The main conclusions of our work are:

1. Magma bodies that feed VEI 6+ eruptions are typically stored at median depths of 3.4-5.1 km, with no clear variation in depth with erupted volume for eruptions with volume

≥ 200 km^3. The shallow location of these magma bodies is consistent with the fact that high-silica rhyolites can only form in the upper crust due to the phase relations in high-silica magmatic systems (Gualda and Ghiorso 2013b). This is also consistent with the fact that exsolved fluids have low density in the upper crust, which helps propel eruptions to the surface. Two smaller eruptions (i.e., < 50 km^3) in the TVZ come from deeper levels (~10-12 km), which may be facilitated by the extensional tectonic environment in the TVZ. The deep origin of these eruptions is also likely linked to their occurrence at the early stages of magmatic cycles in two different volcanic centers of the TVZ.

2. For eruptions with volumes > 50 km^3, thicknesses are typically in the range of 1.5 to 4 km, irrespective of erupted volume. The two smaller eruptions from the TVZ (Chimp and Taupō) are characterized by much smaller calculated thicknesses (≤1.5 km).
3. In combination, this suggests that the interval between 3 and 5 km depth in the shallow crust is the most favorable for the accumulation of large volumes of magma, and it may also suggest that there are crustal or magmatic controls on the maximum thickness of magma bodies that feed large-scale eruptions. Constraints on the thicknesses and locations of ancient melt-dominated magma may help guide geophysical studies aimed at identifying and imaging current magmatic systems.
4. Comparison of magma body thicknesses calculated using geobarometry with volume:area values suggests that most magmas that feed VEI 6+ eruptions are found in melt-dominated bodies of magma, rather than such eruptions being fed by rapid mobilization (on eruption timescales) of melt dispersed in large volumes of magma mush.

5. While magma body thickness shows a positive correlation with volume for erupted volumes up to 50 km^3, no systematic trend is observed for larger volumes, and thicknesses for magma bodies feeding eruptions with 200-1,500 km^3 have the same range of thicknesses. This suggests that the growth of bodies of magma that feed supereruptions takes place via lateral spreading with increasing aspect ratio of the magma bodies involved in such eruptions.

Our study of Quaternary deposits of silicic VEI 6+ eruptions reveals important general patterns regarding the architecture of the magmatic systems that cause very large and supereruption-forming volcanic events. Many of the characteristics outlined above suggest that the behavior of magmatic systems shifts when magma volume reaches ~200 km^3, such that the mechanisms of magma accumulation, pre-eruptive storage and eruption for events ≥ 200 km^3 are distinct than those for smaller events. Given that eruptions of such magnitude have not been observed using modern scientific methods, efforts like ours focusing on the study of the geological record are the only source of information for such geologically important and potentially societally impactful events. While the data presented here provide rich information on the level of pre-eruptive storage, further work is necessary to better characterize deeper crustal levels where magma is located prior to pre-eruptive storage.

6. Funding declaration

Research presented here benefited from funding to Gualda provided by the USA National Science Foundation through awards EAR-1830122 and EAR-1151337 and by the Japan Nuclear Regulatory Authority.

7. References

Acocella V (2007) Understanding caldera structure and development: An overview of analogue models compared to natural calderas. Earth-Science Reviews 85:125–160. https://doi.org/10.1016/j.earscirev.2007.08.004

Allan ASR, Barker SJ, Millet MA, et al (2017) A cascade of magmatic events during the assembly and eruption of a super-sized magma body. Contributions to Mineralogy and Petrology 172:. https://doi.org/10.1007/s00410-017-1367-8

Allan ASR, Morgan DJ, Wilson CJN, Millet MA (2013) From mush to eruption in centuries: assembly of the super-sized Oruanui magma body. Contrib Mineral Petrol 166:143–164. https://doi.org/10.1007/s00410-013-0869-2

Anderson AT, Davis AM, Lu FQ (2000) Evolution of Bishop Tuff rhyolitic magma based on melt and magnetite inclusions and zoned phenocrysts. Journal of Petrology 41:449–473

Bachmann O, Huber C (2016) Silicic magma reservoirs in the Earth's crust. American Mineralogist 101:2377–2404. https://doi.org/10.2138/am-2016-5675

Bachmann O, Huber C (2019) The Inner Workings of Crustal Distillation Columns; the Physical Mechanisms and Rates Controlling Phase Separation in Silicic Magma Reservoirs. Journal of Petrology 60:3–18. https://doi.org/10.1093/petrology/egy103

Bailey RA, Dalrymple GB, Lanphere MA (1976) Volcanism, structure, and geochronology of Long-Valley Caldera, Mono-County, California. Journal of Geophysical Research 81:725–744

Bégué F, Deering CD, Gravley DM, et al (2014a) Extraction, Storage and Eruption of Multiple Isolated Magma Batches in the Paired Mamaku and Ohakuri Eruption, Taupo Volcanic Zone, New Zealand. Journal of Petrology 55:1653–1684. https://doi.org/10.1093/petrology/egu038

Bégué F, Gualda GAR, Ghiorso MS, et al (2014b) Phase-equilibrium geobarometers for silicic rocks based on rhyolite-MELTS. Part 2: application to Taupo Volcanic Zone rhyolites. Contributions to Mineralogy and Petrology 168:. https://doi.org/10.1007/s00410-014-1082-7

Beresford SW, Cole JW (2000) Kaingaroa Ignimbrite, Taupo Volcanic Zone, New Zealand: Evidence for asymmetric caldera subsidence of the Reporoa Caldera. New Zealand Journal of Geology and Geophysics 43:471–481. https://doi.org/10.1080/00288306.2000.9514903

Biondi E, Zhu W, Li J, et al (2023) An upper-crust lid over the Long Valley magma chamber. Science Advances 9:eadi9878. https://doi.org/10.1126/sciadv.adi9878

Black BA, Andrews BJ (2020) Petrologic imaging of the architecture of magma reservoirs feeding caldera-forming eruptions. Earth and Planetary Science Letters 552:116572. https://doi.org/10.1016/j.epsl.2020.116572

Blundy J, Cashman K (2001) Ascent-driven crystallisation of dacite magmas at Mount St Helens, 1980-1986. Contrib Mineral Petrol 140:631–650

Brown SJA, Wilson CJN, Cole JW, Wooden J (1998) The Whakamaru group ignimbrites, Taupo Volcanic Zone, New Zealand: evidence for reverse tapping of a zoned silicic magmatic system. Journal of Volcanology and Geothermal Research 84:1–37. https://doi.org/10.1016/s0377-0273(98)00020-1

Bryan SE, Peate IU, Peate DW, et al (2010) The largest volcanic eruptions on Earth. Earth-Science Reviews 102:207–229. https://doi.org/10.1016/j.earscirev.2010.07.001

Cashman KV, Giordano G (2014) Calderas and magma reservoirs. Journal of Volcanology and Geothermal Research 288:28–45. https://doi.org/10.1016/j.jvolgeores.2014.09.007

Cooper GF, Wilson CJN, Millet M-A, et al (2012) Systematic tapping of independent magma chambers during the 1 Ma Kidnappers supereruption. Earth and Planetary Science Letters 313:. https://doi.org/10.1016/j.epsl.2011.11.006

Cooper KM, Kent AJR (2014) Rapid remobilization of magmatic crystals kept in cold storage. Nature 506:480-+. https://doi.org/10.1038/nature12991

Davy BW, Caldwell TG (1998) Gravity, magnetic and seismic surveys of the caldera complex, Lake Taupo, North Island, New Zealand. Journal of Volcanology and Geothermal Research 81:69–89. https://doi.org/10.1016/S0377-0273(97)00074-7

Delph JR, Ward KM, Zandt G, et al (2017) Imaging a magma plumbing system from MASH zone to magma reservoir. Earth and Planetary Science Letters 457:313–324. https://doi.org/10.1016/j.epsl.2016.10.008

Duan C, Song W, Schmandt B, et al (2025) A sharp volatile-rich cap to the Yellowstone magmatic system. Nature 640:962–966. https://doi.org/10.1038/s41586-025-08775-9

Flanagan FJ (1976) Descriptions and analyses of eight new USGS rock standards. US Geological Survey Professional Paper 840:192 p.

Geshi N, Yamada I, Matsumoto K, et al (2020) Accumulation of rhyolite magma and triggers for a caldera-forming eruption of the Aira Caldera, Japan. Bull Volcanol 82:44. https://doi.org/10.1007/s00445-020-01384-6

Ghiorso MS, Gualda GAR (2015) An H2O-CO2 mixed fluid saturation model compatible with rhyolite-MELTS. Contributions to Mineralogy and Petrology 169:. https://doi.org/10.1007/s00410-015-1141-8

Gladney ES, Roelandts I (1988) 1987 compilation of elemental concentration data for USGS BHVO-1, MAG-1, QLO-1, RGM-1, SCo-1, SDC-1, SGR-1, and STM-1. Geostandards Newsletter 12:253–362. https://doi.org/10.1111/j.1751-908X.1988.tb00053.x

Gravley DM, Deering CD, Leonard GS, Rowland JV (2016) Ignimbrite flare-ups and their drivers: A New Zealand perspective. Earth-Science Reviews 162:65–82. https://doi.org/10.1016/j.earscirev.2016.09.007

Gravley DM, Hasegawa T, Mochizuki N, et al (2025) A new paleomagnetic constraint on the duration of a twin caldera-forming eruption sequence: a potential solution to an enduring problem in decoding >VEI 7 eruption timescales. Earth Planets Space 77:106. https://doi.org/10.1186/s40623-025-02179-9

Gravley DMc (2004) The Ohakuri pyroclastic deposits and the evolution of the Rotorua-Ohakuri volcanotectonic depression. University of Canterbury. Geological Science

Gualda GAR, Begue F, Pamukçu AS, Ghiorso MS (2019a) Rhyolite-MELTS vs DERP-Newer Does not Make it Better: a Comment on “The Effect of Anorthite Content and Water on Quartz-Feldspar Cotectic Compositions in the Rhyolitic System and Implications for Geobarometry” by Wilke et al. (2017; Journal of Petrology, 58, 789-818). Journal of Petrology 60:855–863. https://doi.org/10.1093/petrology/egz003

Gualda GAR, Frontoni A, Wallrich BM, et al (revised) An assessment of the quality of microanalysis of silicate glass using scanning electron microscope-based energy dispersive spectrometry (SEM-EDS). American Mineralogist

Gualda GAR, Ghiorso MS (2013a) The Bishop Tuff giant magma body: an alternative to the Standard Model. Contributions to Mineralogy and Petrology 166:755–775. https://doi.org/10.1007/s00410-013-0901-6

Gualda GAR, Ghiorso MS (2014) Phase-equilibrium geobarometers for silicic rocks based on rhyolite-MELTS. Part 1: Principles, procedures, and evaluation of the method. Contributions to Mineralogy and Petrology 168:1033. https://doi.org/10.1007/s00410-014-1033-3

Gualda GAR, Ghiorso MS (2013b) Low-Pressure Origin of High-Silica Rhyolites and Granites. Journal of Geology 121:537–545. https://doi.org/10.1086/671395

Gualda GAR, Ghiorso MS, Hurst AA, et al (2022) A complex patchwork of magma bodies that fed the Bishop Tuff supereruption (Long Valley Caldera, CA, United States): Evidence from matrix glass major and trace-element compositions. Front Earth Sci 10:798387. https://doi.org/10.3389/feart.2022.798387

Gualda GAR, Gravley DM, Deering CD, Ghiorso MS (2019b) Magma extraction pressures and the architecture of volcanic plumbing systems. Earth and Planetary Science Letters 522:118–124. https://doi.org/10.1016/j.epsl.2019.06.020

Gualda GAR, Grayley DM, Connor M, et al (2018) Climbing the crustal ladder: Magma storage-depth evolution during a volcanic flare-up. Science Advances 4:eaap7567. https://doi.org/10.1126/sciadv.aap7567

Gualda GAR, Pamukçu AS, Ghiorso MS, et al (2012) Timescales of quartz crystallization and the longevity of the Bishop giant magma body. Plos One 7:e37492. https://doi.org/10.1371/journal.pone.0037492

Gualda GAR, Sutton SR (2016) The Year Leading to a Supereruption. PLoS ONE 11:e0159200. https://doi.org/10.1371/journal.pone.0159200

Harmon LJ, Cowlyn J, Gualda GAR, Ghiorso MS (2018) Phase-equilibrium geobarometers for silicic rocks based on rhyolite-MELTS. Part 4: Plagioclase, orthopyroxene, clinopyroxene, glass geobarometer, and application to Mt. Ruapehu, New Zealand. Contributions to Mineralogy and Petrology 173:. https://doi.org/10.1007/s00410-017-1428-z

Harmon LJ, Gualda GAR, Gravley DM, et al (2024a) The Whakamaru magmatic system (Taupō Volcanic Zone, New Zealand), part 1: Evidence from tephra deposits for the eruption of multiple magma types through time. Journal of Volcanology and Geothermal Research 445:107966. https://doi.org/10.1016/j.jvolgeores.2023.107966

Harmon LJ, Gualda GAR, Wallrich BM, Miller CF (2025) Shallow storage conditions at Krafla IDDP-1 revealed by rhyolite-MELTS geobarometry, and implications for global shallow magmatism. Earth and Planetary Science Letters 663:119421. https://doi.org/10.1016/j.epsl.2025.119421

Harmon LJ, Smithies SL, Gualda GAR, Gravley DM (2024b) The Whakamaru magmatic system (Taupō Volcanic Zone, New Zealand), part 2: Evidence from ignimbrite deposits for the pre-eruptive distribution of melt-dominated magma and magma mush. Journal of Volcanology and Geothermal Research 447:108013. https://doi.org/10.1016/j.jvolgeores.2024.108013

Hasegawa T, Mochizuki N, Shibuya H, et al (2024) Paleomagnetic study of the 30 ka Aira caldera-forming eruption and 60–45 ka Iwato pyroclastic flow deposits, southern Kyushu, Japan. Earth Planets Space 76:161. https://doi.org/10.1186/s40623-024-02089-2

Hildreth W (1979) The Bishop Tuff: Evidence for the origin of compositional zonation in silicic magma chambers. Geological Society of America Special Paper 180:43–75

Hildreth W, Mahood GA (1986) Ring-fracture eruption of the Bishop Tuff. Geological Society of America Bulletin 97:396–403

Hildreth W, Wilson CJN (2007) Compositional zoning of the Bishop Tuff. J Petrol 48:951–999. https://doi.org/10.1093/petrology/egm007

Hogg AG, Wilson CJN, Lowe DJ, et al (2019) Wiggle-match radiocarbon dating of the Taupo eruption. Nat Commun 10:4669. https://doi.org/10.1038/s41467-019-12532-8

Huang H-H, Lin F-C, Schmandt B, et al (2015) The Yellowstone magmatic system from the mantle plume to the upper crust. Science 348:773–776. https://doi.org/10.1126/science.aaa5648

Huber C, Townsend M, Degruyter W, Bachmann O (2019) Optimal depth of subvolcanic magma chamber growth controlled by volatiles and crust rheology. Nat Geosci 12:762–768. https://doi.org/10.1038/s41561-019-0415-6

Ikeda Y (1991) Geochemistry and magmatic evolution of Pliocene-early Pleistocene pyroclastic flow deposits in central Hokkaido, Japan. Jour Geol Soc Japan 97:645–666. https://doi.org/10.5575/geosoc.97.645

Ikeda Y, Mukoyama S (1983) Stratigraphy and correlation of the pyroclastic flow deposits in the Furano-Asahikawa area, central Hokkaido, Japan. Jour Geol Soc Japan 89:163–172. https://doi.org/10.5575/geosoc.89.163

Ishii E, Nakagawa M, Saito H, Yamamoto A (2008) The Pleistocene Tokachimitsumata caldera and associated pyroclastic flow deposits in central Hokkaido, Japan: Correlation of large-scale pyroclastic flow deposits with source calderas. Jour Geol Soc Japan 114:348–365. https://doi.org/10.5575/geosoc.114.348

Jellinek AM, DePaolo DJ (2003) A model for the origin of large silicic magma chambers: precursors of caldera-forming eruptions. Bull Volcanol 65:363–381. https://doi.org/10.1007/s00445-003-0277-y

Johannes W, Holtz F (1996) Petrogenesis and experimental petrology of granitic rocks. Springer, Berlin

Karlstrom L, Dufek J, Manga M (2010) Magma chamber stability in arc and continental crust. Journal of Volcanology and Geothermal Research 190:249–270. https://doi.org/10.1016/j.jvolgeores.2009.10.003

Klein BZ, Eddy MP (2024) What’s in an age? Calculation and interpretation of ages and durations from U-Pb zircon geochronology of igneous rocks. GSA Bulletin 136:93–109. https://doi.org/10.1130/B36686.1

Kuritani T (2023) Geochemical constraints on the evolution of the magmatic system leading to catastrophic eruptions at Aira Caldera, Japan. Lithos 450–451:107208. https://doi.org/10.1016/j.lithos.2023.107208

Leonard GS, Begg JG, Wilson CJN (2010) Geology of the Rotorua area. Institute of Geological and Nuclear Sciences, Lower Hutt

Liu Y, Anderson AT, Wilson CJN, et al (2006) Mixing and differentiation in the Oruanui rhyolitic magma, Taupo, New Zealand: evidence from volatiles and trace elements in melt inclusions. Contributions to Mineralogy and Petrology 151:71–87. https://doi.org/10.1007/s00410-005-0046-3

Lowenstern JB, Smith RB, Hill DP (2006) Monitoring super-volcanoes: geophysical and geochemical signals at Yellowstone and other large caldera systems. Philosophical Transactions of the Royal Society a-Mathematical Physical and Engineering Sciences 364:2055–2072. https://doi.org/10.1098/rsta.2006.1813

Lubbers J, Kent AJR, De Silva S (2022) Thermal Budgets of Magma Storage Constrained by Diffusion Chronometry: the Cerro Galán Ignimbrite. Journal of Petrology 63:egac048. https://doi.org/10.1093/petrology/egac048

Maguire R, Schmandt B, Chen M, et al (2022) Resolving Continental Magma Reservoirs With 3D Surface Wave Tomography. Geochem Geophys Geosyst 23:e2022GC010446. https://doi.org/10.1029/2022GC010446

Matthews NE, Huber C, Pyle DM, Smith VC (2012) Timescales of Magma Recharge and Reactivation of Large Silicic Systems from Ti Diffusion in Quartz. Journal of Petrology 53:1385–1416. https://doi.org/10.1093/petrology/egs020

Miller AL, Barker SJ, Wilson CJN (2026) Reconstructing one of the largest explosive eruptions of the Quaternary through high-resolution tephra geochemistry: the 349 ka Whakamaru supereruption. Journal of Volcanology and Geothermal Research 474:108619. https://doi.org/10.1016/j.jvolgeores.2026.108619

Miller CF, Wark DA (2008) Supervolcanoes and their explosive supereruptions. Elements 4:11–15. https://doi.org/10.2113/gselements.4.1.11

Mullet B, Segall P, Fávero Neto AH (2023) Numerical modeling of caldera formation using Smoothed Particle Hydrodynamics (SPH). Geophysical Journal International 234:887–902. https://doi.org/10.1093/gji/ggad084

Myers ML, Wallace PJ, Wilson CJN (2019) Inferring magma ascent timescales and reconstructing conduit processes in explosive rhyolitic eruptions using diffusive losses of hydrogen from melt inclusions. Journal of Volcanology and Geothermal Research 369:95–112. https://doi.org/10.1016/j.jvolgeores.2018.11.009

Nagaoka S, Okuno M, Arai F (2001) Tephrostratigraphy and eruptive history of the Aira caldera volcano during 100-30ka, Kyushu, Japan. Jour Geol Soc Japan 107:432–450. https://doi.org/10.5575/geosoc.107.432

Newhall CG, Self S (1982) The Volcanic Explosivity Index (VEI): An estimate of explosive magnitude for historical volcanism. J Geophys Res-Oceans 87:1231–1238. https://doi.org/10.1029/JC087iC02p01231

Nishihara A, Tatsumi Y, Kaneko K, et al (2024) Voluminous magma formation for the 30-ka Aira caldera-forming eruption in SW Japan: contributions of crust-derived felsic and mafic magmas. Front Earth Sci 11:1283844. https://doi.org/10.3389/feart.2023.1283844

Nishike K, Ishige K, Shimada S, Nakagawa M (2017) Fission-track and U-Pb Dating of Pyroclastic Flow Deposits Around Tokachi Caldera in the Biei and Kamikawa Areas of Central Hokkaido, Japan. Bulletin of the Volcanological Society of Japan 62:83–94. https://doi.org/10.18940/kazan.62.2_83

Pamukçu AS, Gualda GAR, Begue F, Gravley DM (2015a) Melt inclusion shapes: Timekeepers of short-lived giant magma bodies. Geology 43:947–950. https://doi.org/10.1130/g37021.1

Pamukçu AS, Gualda GAR, Ghiorso MS, et al (2015b) Phase-equilibrium geobarometers for silicic rocks based on rhyolite-MELTS-Part 3: Application to the Peach Spring Tuff (Arizona-California-Nevada, USA). Contributions To Mineralogy and Petrology 169:. https://doi.org/10.1007/s00410-015-1122-y

Pamukçu AS, Gualda GAR, Gravley DM (2021) Rhyolite-MELTS and the storage and extraction of large-volume crystal-poor rhyolitic melts at the Taupō Volcanic Center: a reply to Wilson et al. (2021). Contrib Mineral Petrol 176:82. https://doi.org/10.1007/s00410-021-01840-2

Pamukçu AS, Wright KA, Gualda GAR, Gravley D (2020) Magma residence and eruption at the Taupo Volcanic Center (Taupo Volcanic Zone, New Zealand): insights from rhyolite-MELTS geobarometry, diffusion chronometry, and crystal textures. Contributions to Mineralogy and Petrology 175:48. https://doi.org/10.1007/s00410-020-01684-2

Paulatto M, Hooft EEE, Chrapkiewicz K, et al (2022) Advances in seismic imaging of magma and crystal mush. Front Earth Sci 10:970131. https://doi.org/10.3389/feart.2022.970131

Pitcher BW, Gualda GAR, Geshi N (2026) Submillennial timescales of eruptible rhyolite magma: Converging evidence from Aira Caldera, Japan. Sci Adv 12:eaea2075. https://doi.org/10.1126/sciadv.aea2075

Pitcher BW, Gualda GAR, Hasegawa T (2021) Repetitive Duality of Rhyolite Compositions, Timescales, and Storage and Extraction Conditions for Pleistocene Caldera-forming Eruptions, Hokkaido, Japan. Journal of Petrology 62:egaa106. https://doi.org/10.1093/petrology/egaa106

Rasht-Behesht M, Huber C, Mancinelli NJ (2020) Detectability of Melt-Rich Lenses in Magmatic Reservoirs From Teleseismic Waveform Modeling. JGR Solid Earth 125:e2020JB020264. https://doi.org/10.1029/2020JB020264

Self S (2006) The effects and consequences of very large explosive volcanic eruptions. Philosophical Transactions of the Royal Society a-Mathematical Physical and Engineering Sciences 364:2073–2097. https://doi.org/10.1098/rsta.2006.1814

Shamloo HI, Till CB (2019) Decadal transition from quiescence to supereruption: petrologic investigation of the Lava Creek Tuff, Yellowstone Caldera, WY. Contributions to Mineralogy and Petrology 174:. https://doi.org/10.1007/s00410-019-1570-x

Sheridan MF (1965) The mineralogy and petrology of the Bishop Tuff. Stanford University

Smith RL, Bailey RA (1968) Resurgent Cauldrons. In: Geological Society of America Memoirs. Geological Society of America, pp 613–662

Smith VC, Staff RA, Blockley SPE, et al (2013) Identification and correlation of visible tephras in the Lake Suigetsu SG06 sedimentary archive, Japan: chronostratigraphic markers for synchronising of east Asian/west Pacific palaeoclimatic records across the last 150 ka. Quaternary Science Reviews 67:121–137. https://doi.org/10.1016/j.quascirev.2013.01.026

Smithies SL, Gualda GAR, Harmon LJ (2025) Phase-equilibrium geobarometers for silicic rocks based on rhyolite-MELTS. Part 5: principles for multiple-phase geobarometry with examples from plagioclase + orthopyroxene ± quartz ± magnetite. Contrib Mineral Petrol 180:88. https://doi.org/10.1007/s00410-025-02274-w

Smithies SL, Harmon LJ, Allen SM, et al (2023) Following magma: The pathway of silicic magmas from extraction to storage during an ignimbrite flare-up, Taupō Volcanic Zone, New Zealand. Earth and Planetary Science Letters 607:118053. https://doi.org/10.1016/j.epsl.2023.118053

Spinks KD, Acocella V, Cole JW, Bassett KN (2005) Structural control of volcanism and caldera development in the transtensional Taupo Volcanic Zone, New Zealand. Journal of Volcanology and Geothermal Research 144:7–22. https://doi.org/10.1016/j.jvolgeores.2004.11.014

Stagpoole V, Miller C, Caratori Tontini F, et al (2021) A two million-year history of rifting and caldera volcanism imprinted in new gravity anomaly compilation of the Taupō Volcanic Zone, New Zealand. New Zealand Journal of Geology and Geophysics 64:358–371. https://doi.org/10.1080/00288306.2020.1848882

Tavazzani L, Peres S, Sinigoi S, et al (2020) Timescales and Mechanisms of Crystal-mush Rejuvenation and Melt Extraction Recorded in Permian Plutonic and Volcanic Rocks of the Sesia Magmatic System (Southern Alps, Italy). Journal of Petrology 61:egaa049. https://doi.org/10.1093/petrology/egaa049

Till CB, Vazquez JA, Boyce JW (2015) Months between rejuvenation and volcanic eruption at Yellowstone caldera, Wyoming. Geology 43:695–698. https://doi.org/10.1130/g36862.1

Tramontano S, Gualda GAR, Ghiorso MS (2017) Internal triggering of volcanic eruptions: tracking overpressure regimes for giant magma bodies. Earth and Planetary Science Letters 472:142–151. https://doi.org/10.1016/j.epsl.2017.05.014

Tuttle OF, Bowen NL (1958) Origin of granite in the light of experimental studies in the system, NaAlSi3O8-KAlSi3O8-SiO2-H2O. Geological Society of America Memoir 74:153

Villamor P, Berryman K (2001) A late Quaternary extension rate in the Taupo Volcanic Zone, New Zealand, derived from fault slip data. New Zealand Journal of Geology and Geophysics 44:243–269. https://doi.org/10.1080/00288306.2001.9514937

Villamor P, Berryman KR, Ellis SM, et al (2017) Rapid Evolution of Subduction-Related Continental Intraarc Rifts: The Taupo Rift, New Zealand. Tectonics 36:2250–2272. https://doi.org/10.1002/2017TC004715

Wallace PJ, Anderson AT, Davis AM (1999) Gradients in H2O, CO2, and exsolved gas in a large-volume silicic magma system: Interpreting the record preserved in melt inclusions from the Bishop Tuff. J Geophys Res-Solid Earth 104:20097–20122

Wendt I, Carl C (1991) The statistical distribution of the mean squared weighted deviation. Chemical Geology: Isotope Geoscience section 86:275–285. https://doi.org/10.1016/0168-9622(91)90010-T

Wilson C, Gravley D, Leonard G, Rowland J (2009) Volcanism in the central Taupo Volcanic Zone, New Zealand: tempo, styles, and controls. Studies in Volcanology: The Legacy of George Walker Special Publications of IAVCEI 2:225–247

Wilson CJN (2001) The 26.5 ka Oruanui eruption, New Zealand: an introduction and overview. Journal of Volcanology and Geothermal Research 112:133–174. https://doi.org/10.1016/s0377-0273(01)00239-6

Wilson CJN (1993) Stratigraphy, chronology, styles and dynamics of late Quaternary eruptions from Taupo volcano, New Zealand. Philosophical Transactions of the Royal Society of London Series A: Physical and Engineering Sciences 343:205–306. https://doi.org/10.1098/rsta.1993.0050

Wilson CJN, Blake S, Charlier BLA, Sutton AN (2006) The 26.5 ka Oruanui eruption, Taupo volcano, New Zealand: Development, characteristics and evacuation of a large rhyolitic magma body. Journal of Petrology 47:35–69

Wilson CJN, Hildreth W (1997) The Bishop Tuff: New insights from eruptive stratigraphy. Journal of Geology 105:407–439

8. Figures

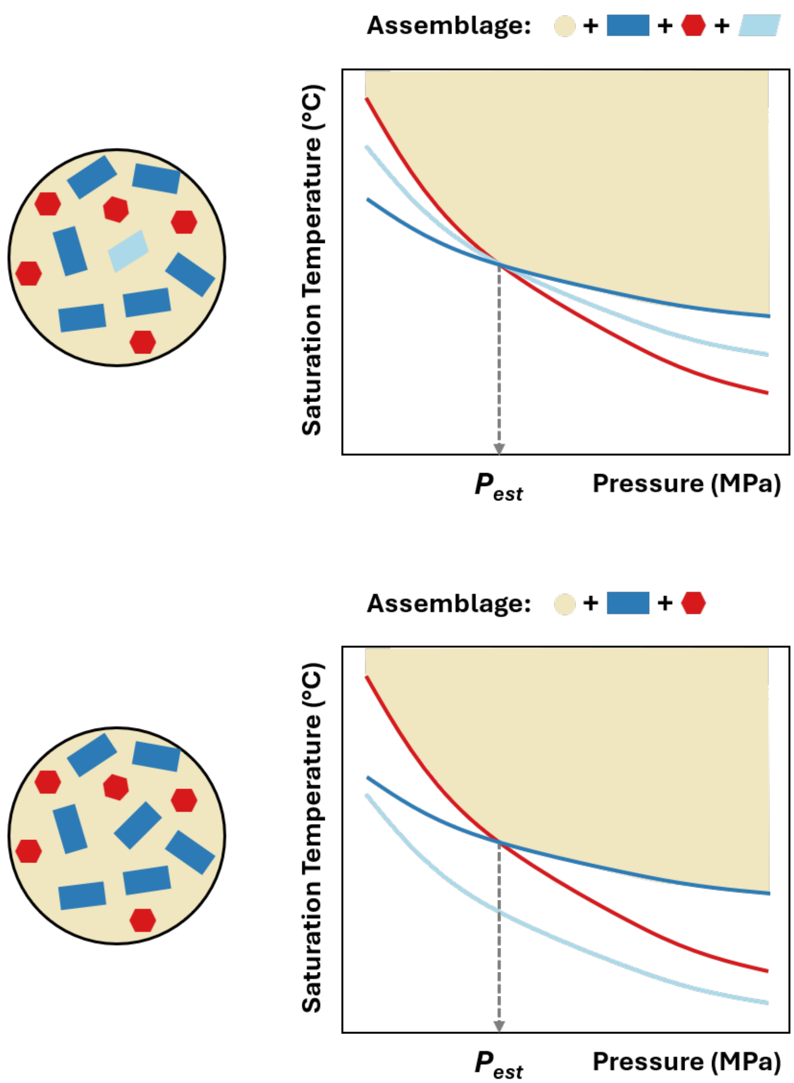

Figure 1. Schematic diagram showing the principles behind rhyolite-MELTS geobarometry. Top diagram shows the case of simultaneous equilibration between melt (in yellowish color) and three mineral phases (dark blue rectangles, red hexagons, and light blue parallelogram), equivalent to the case of quartz and two feldspars. Bottom diagram shows the case of simultaneous equilibration between melt (yellow) and two mineral phases (dark blue and red), equivalent to the case of quartz and one feldspar. In both cases, we seek the condition in which

melt of the given composition (yellow region) appears in simultaneous equilibrium with all mineral phases present in the observed assemblage, which is only possible at the pressure marked as P_{est}.

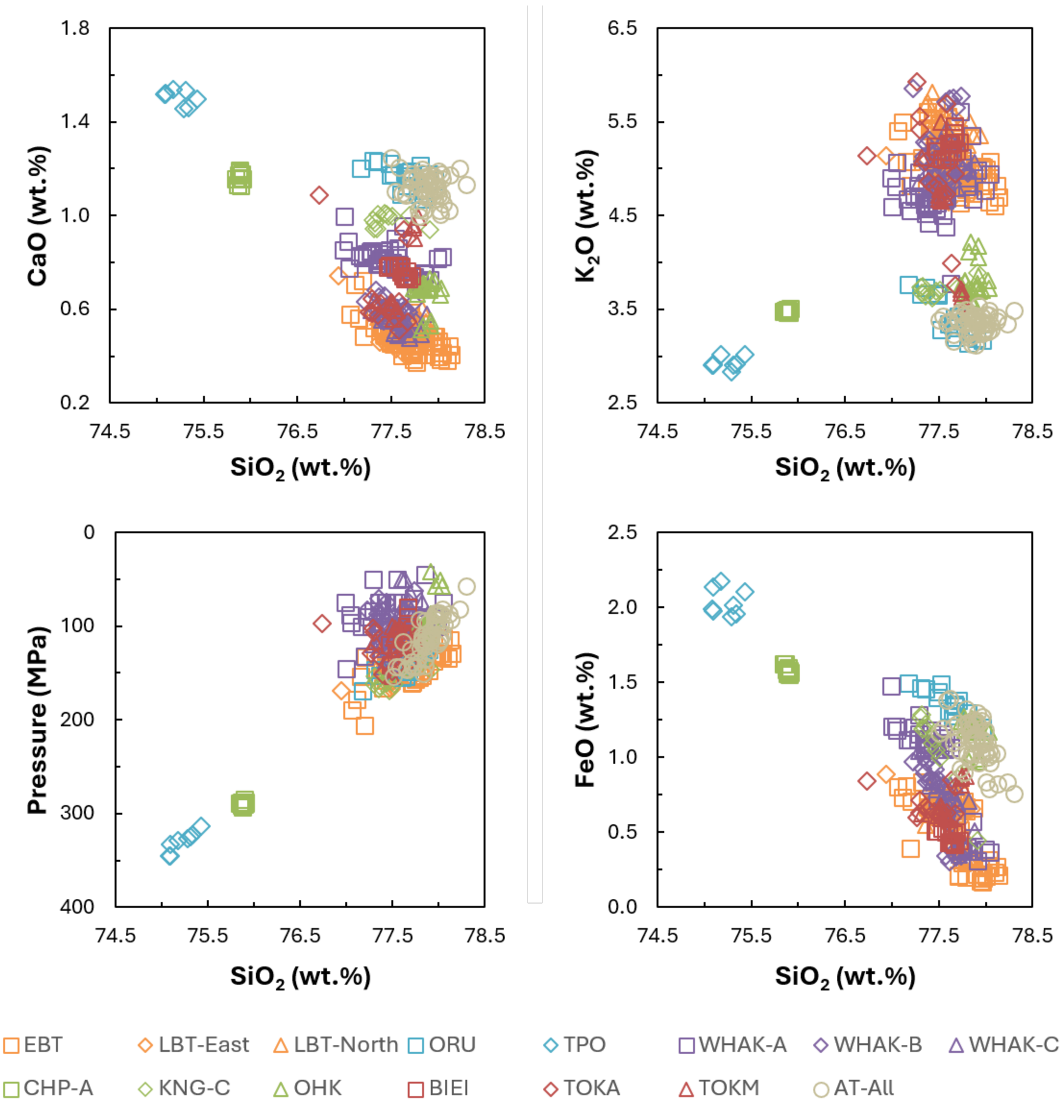

Figure 2. Harker diagrams showing matrix-glass compositions and corresponding rhyolite-MELTS pressures for the units studied here. Only compositions that yield rhyolite-MELTS pressures are shown. Compositions are all rhyolites, with the majority corresponding to high-silica rhyolites. Low K_2O compositions are characteristic of units characterized exclusively by a quartz and plagioclase assemblage. CaO and FeO values separate the compositions into various subgroups. Rhyolite-MELTS pressures broadly correlate with SiO_2, as previously shown (e.g., Gualda and Ghiorso 2013b, 2014).

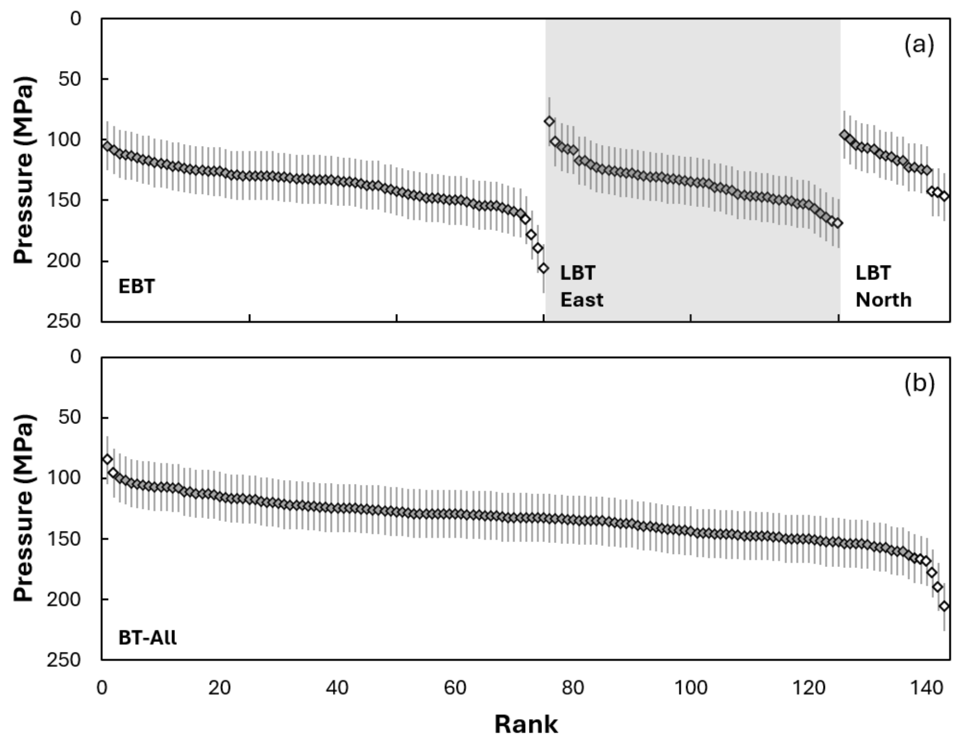

Figure 3. Rank-order diagrams showing results for the Bishop Tuff. (a) Results separated into 3 subunits: early-erupted deposits (EBT), southern and eastern late-erupted deposits (LBT-East), and northern late-erupted deposits (LBT-North). (b) All results for the Bishop Tuff in combination. Outliers are indicated by white fill; error bars are 20 MPa. Depths and thicknesses are similar for the 3 subunits, and the combined dataset suggests all magmas were located at a single crustal level.

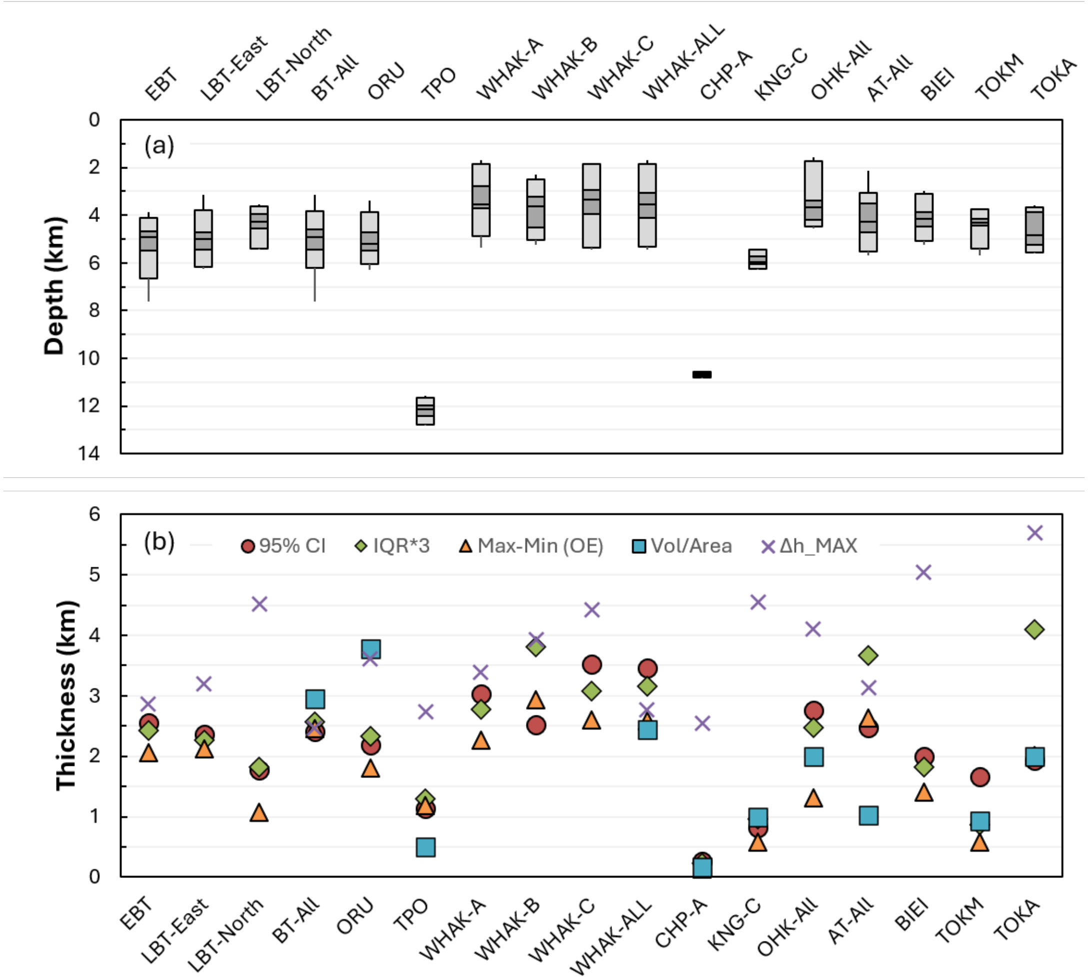

*Figure 4. Summary diagrams showing the depths and thicknesses of magma bodies that fed Quaternary VEI 6+ eruptions included in this study. (a) Box and whisker diagram showing magma depth distribution for all studied units; inner, darker gray box encompasses the 25th to 75th percentiles, with the median shown as a solid line within it; outer, lighter gray box shows the 2.5th and 97.5th percentiles; whiskers extend to minimum and maximum values. (b) Diagram showing magma thicknesses calculated from the pressure data, converted to depth; three different estimates are shown ("95% CI", "IQR*3", and "Max-Min [OE]"), as well as the maximum bound given by* Δh^{MAX}*; volume:area values are shown where appropriate. See text for details. Data for the Taupō and Chimp Ignimbrites suggest these eruptions tapped deeper,*

thinner magma bodies. Data for the Kaingaroa Ignimbrite reveals tapping of a shallow, thin magma body. Other units suggest tapping of magmas primarily located between 2 and 7 km, with median depths between 3 and 6 km, with calculated thicknesses between 1 and 4 km.

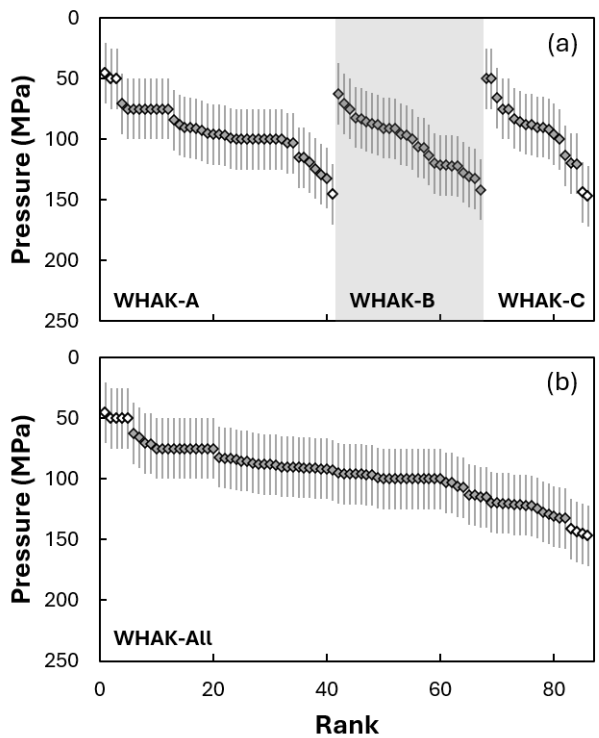

Figure 5. Summary of results for the Whakamaru Group Ignimbrites. (a) Results subdivided into types A, B, and C of Brown et al. (1998). (b) All results shown in combination. Symbols as in Figure 3. Error bars are 25 MPa. Data are consistent with shallow crustal storage at a single level.

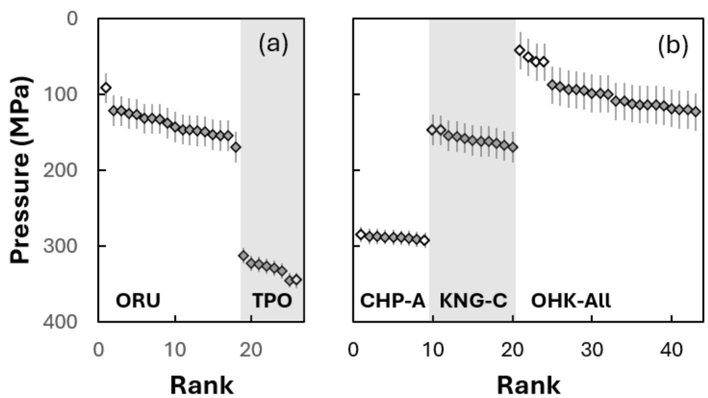

Figure 6. *Summary of results for the Taupō Volcanic Center (a) and the TVZ Flare-Up (b). Symbols as in Figure 3. Error bars 20 MPa for the Oruanui Ignimbrite, 10 MPa for the Taupō Ignimbrite, 10 MPa for the Chimp Ignimbrite type A (CHP-A), 20 MPa for the Kaingaroa Ignimbrite type C (KNG-C), and 25 MPa for the Ohakuri Ignimbrite (OHK). Data for the Taupō and Chimp Ignimbrites suggest tapping of deep and thin magmas; the Kaingaroa Ignimbrite reveals a thin magma body at shallow pressures; finally, the data for the Ohakuri Ignimbrite suggest a thicker shallow magma body. See text for details.*

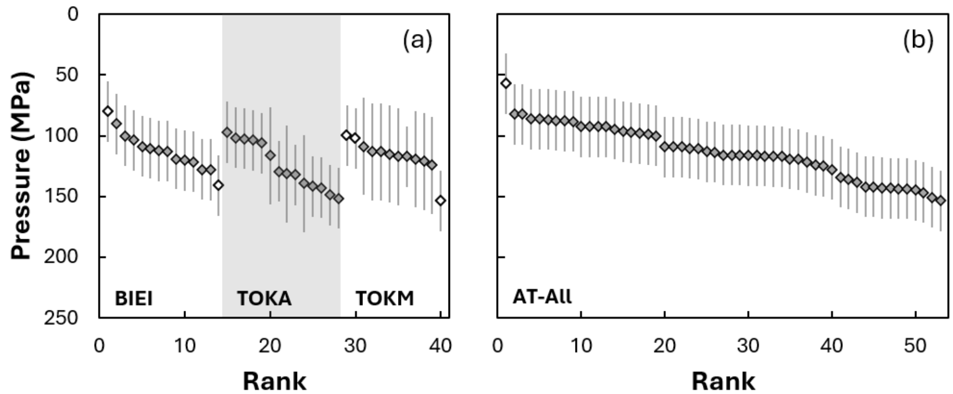

Figure 7. Summary of results for ignimbrites from Central Hokkaido (a) and deposits from the AT eruption (b). (a) Results for the Biei Ignimbrite (BIEI), Tokachi Ignimbrite (TOKA), and Tokachi-Mitsumata Ignimbrite (TOKM). (b) Results for the AT eruption shown in combination. Symbols as in Figure 3. Error bars in (a) are 25 MPa for Q2F pressures and 40 MPa for Q1F pressures. All magmas in Central Hokkaido erupted from similar shallow crustal levels. Error bars in (b) are 25 MPa. Data are consistent with tapping of shallow magma for the AT eruption.

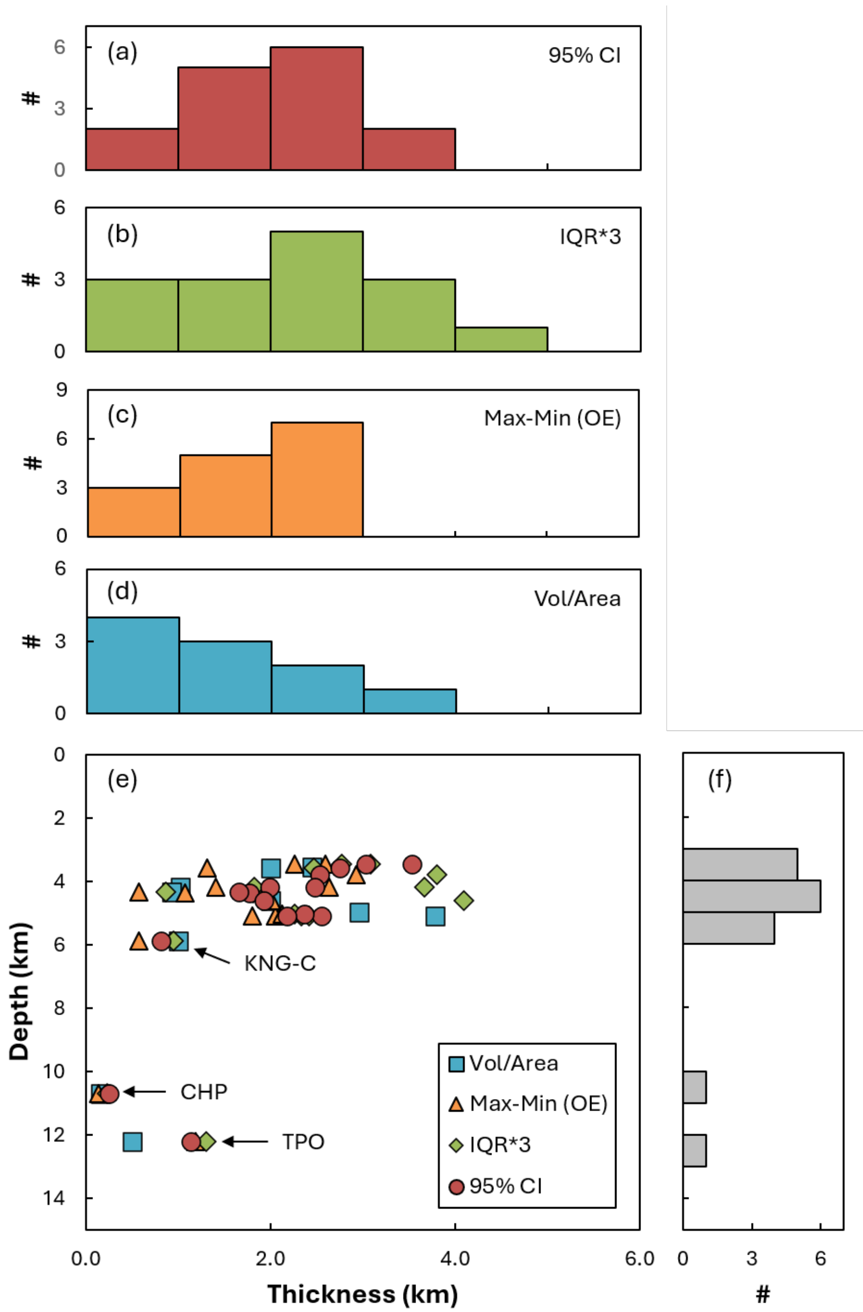

1091

1092 *Figure 8. Diagrams showing the calculated depths and thicknesses of magma bodies that fed*
1093 *Quaternary VEI 6+ eruptions included in this study. (a-c) Histograms showing the distribution of*
1094 *calculated thicknesses. (d) Histogram showing the distribution of volume:area values. (e) Binary*
1095 *diagram showing calculated depths versus calculated thicknesses. (f) Histogram showing the*

distribution of calculated median depth values. Data suggest magmas predominantly erupted from depths of 3-6 km, from magma bodies with thicknesses between 0.5 and 4 km.

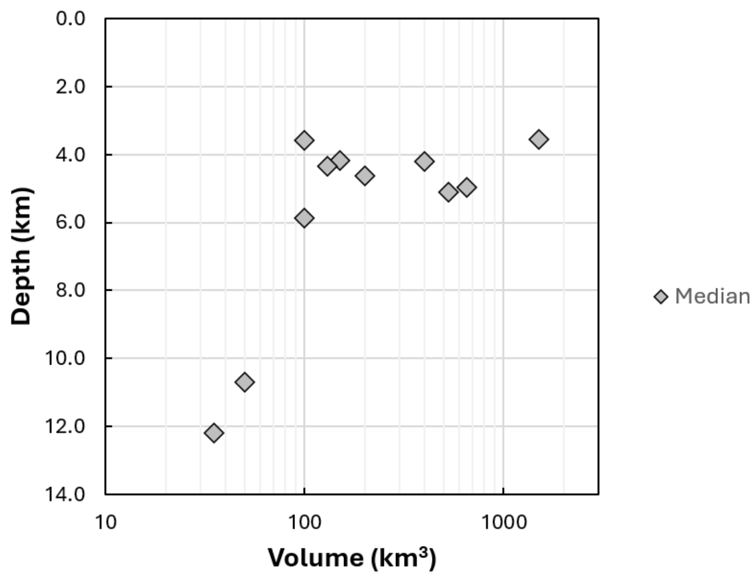

Figure 9. Binary diagram showing the relationship between calculated depth and observed erupted volume. For relatively small volumes (the 35 km^3 Taupō Ignimbrite and the 50 km^3 Chimp Ignimbrite), erupted magma was stored at deeper crustal levels (median depths of 10.7 and 12.2 km). For volumes ≥ 100 km^3, median depth is not a function of volume, with median depths between 3.6 and 5.9 km.

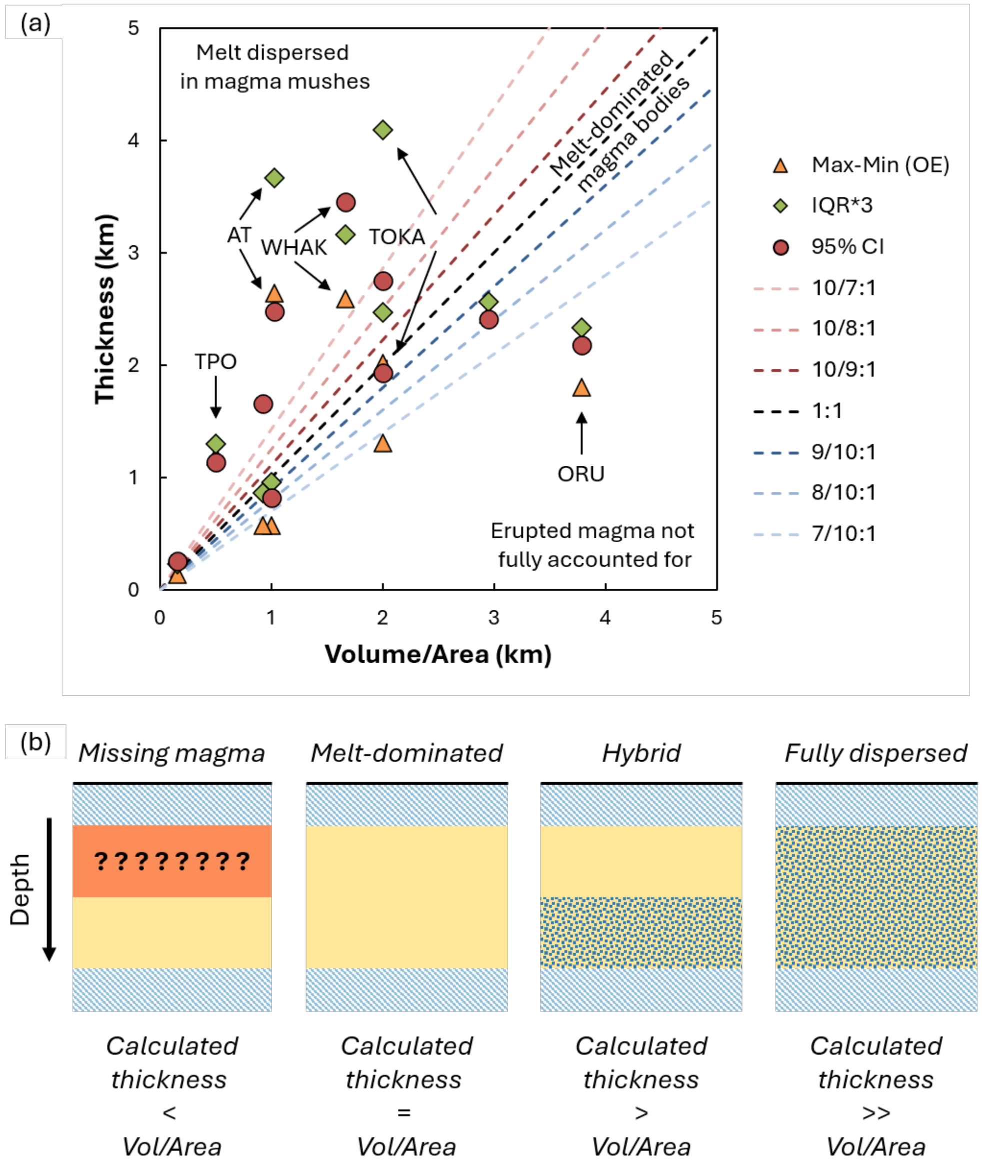

Figure 10. Binary diagram and schematic showing possible relationships between calculated thickness and volume:area values. (a) Binary diagram showing the relationship between calculated thicknesses and volume:area values. Black dashed line shows 1:1 relationship, in which calculated thickness is equal to volume:area value. Below the 1:1 line, the volume:area value is larger than the calculated thickness, suggesting that not all erupted magma has been accounted for in our sampling. Above the 1:1 line, the region from which magma was tapped is

*larger than what can be explained by the volume:area value, suggesting that magma may have been dispersed within more crystal-rich material. Blue and red dashed lines show different values of the ratio between thickness and volume:area value. The Oruanui Ignimbrite is the main example of a case in which the distribution of pressures in our dataset cannot explain the observed volume:area value. The Taupō Ignimbrite and AT Eruption are the clearest examples of magma that may have been dispersed within more crystal-rich material. Data for the Tokachi Ignimbrite is ambiguous, but only the IQR*3 calculated thickness falls away from the 1:1 line, suggesting that it is unlikely that it represents an example of eruption of melt dispersed in crystal-rich magma mush. (b) Schematic diagrams showing the possible pre-eruptive configurations. Melt-dominated magma bodies shown in yellow; magma not sampled is shown in orange with question marks; blue diagonally hatched domains represent country rocks; coarse-dotted domains with yellow background represent magma mush with interstitial melt. Evidence suggests that most Quaternary VEI 6+ eruptions studied here tapped melt-dominated magma bodies.*

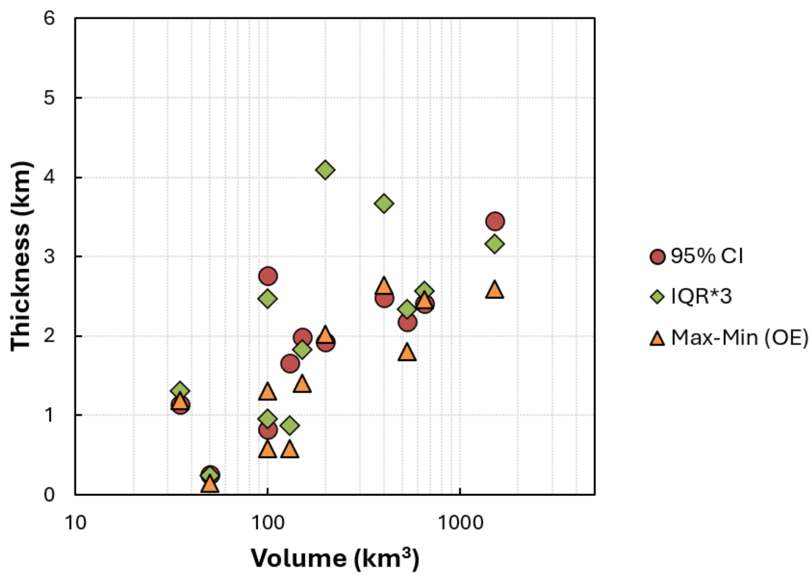

Figure 11. Binary diagram showing the relationship between calculated thicknesses and volume. Thickness increases with volume for volumes < 200 km^3, with significant scatter for volumes of ~200 km^3. For larger volumes, there is limited or no increase in thickness with volume. This suggests that, for volumes > 200 km^3, growth of magma bodies takes place by lateral spreading.

9. Tables

Table 1. Characteristics of the eruptive units that are part of this study.

Deposit	**Volume** *(km^3)*	**Reference**	**Area** *(km^2)*	**Reference**	**Volume/Area** *(km)*	**Assemblage**
Bishop Tuff	650	Wilson & Hildreth (1997)	220	Wilson & Hildreth (1997)	3.0	Q2F
Oruanui Ignimbrite	530	Wilson (2001)	140	Wilson (2001)	3.8	Q1F
Taupō Ignimbrite	35	Wilson (1993)	70	Davy & Caldwell (1998)	0.5	Q1F
Whakamaru Group Ignimbrites	1,500	Miller et al. (2026)	900	Leonard et al. (2010)	2.4	Q1F+Q2F
Chimp Ignimbrite	50	Wilson et al. (2009)	310	Stagpoole et al. (2021)	0.2	Q1F
Kaingaroa Ignimbrite	100	Beresford & Cole (2000)	100	Stagpoole et al. (2021)	1.0	Q1F
Ohakuri Ignimbrite	100	Gravley (2004)	50	Leonard et al.	2.0	Q1F
AT Eruption	400	Geshi et al. (2020)	390	Geshi et al. (2020)	1.0	Q1F
Biei Ignimbrite	150	Ikeda (1991)	-		-	Q1F
Tokachi Ignimbrite	200	Nishiki et al. (2017)	100	Nishiki et al. (2017)	2.0	Q1F+Q2F
Tokachi-Mitsumata Ignimbrite	130	Ishii et al. (2008)	140	Ishii et al. (2008)	0.9	Q1F+Q2F

Table 2. Summary of thicknesses and related quantities for the eruptive units that are part of this study

	EBT	LBT-East	LBT-North	BT-All	WHAK-A	WHAK-B	WHAK-C	WHAK-All
n	75	50	18	143	41	26	19	86
σ (MPa)	25	25	25	25	25	25	25	25
MSWD	0.50	0.47	0.35	0.53	0.72	0.71	1.13	0.82
MSWD [σ=20 MPa]	0.78	0.74	0.55	0.83	-	-	-	-
Threshold (+)	1.33	1.40	1.69	1.24	1.45	1.57	1.67	1.31
Threshold (-)	0.67	0.60	0.31	0.76	0.55	0.43	0.33	0.69
ΔhMAX (km)	2.9	3.2	4.5	2.5	3.4	3.9	4.4	2.8
ΔhMAX [σ=20 MPa] (km)	2.3	2.6	3.6	2.0	-	-	-	-
95% CI (km)	2.6	2.4	1.8	2.4	3.0	2.5	3.5	3.5
IQR*3 (km)	2.4	2.3	1.8	2.6	2.8	3.8	3.1	3.2
Max-Min [OE] (km)	2.1	2.1	1.1	2.5	2.3	2.9	2.6	2.6
Vol/Area (km)	-	-	-	3.0	-	-	-	2.4

	ORU	TPO	CHP-A	KNG-C	OHK-All	BIEI	TOKA	TOKM	ITO-All
n	18	8	9	11	23	14	14	12	53
σ (MPa)	20	10	10	20	25	25	28	35	25
MSWD	0.77	1.22	0.05	0.14	0.89	0.41	0.58	0.28	0.77
MSWD [σ=20 MPa]	-	-	-	-	-	-	-	-	-
Threshold (+)	1.69	2.07	2.00	1.89	1.60	1.78	1.78	1.85	1.39
Threshold (-)	0.31	0.00	0.00	0.11	0.40	0.22	0.22	0.15	0.61
ΔhMAX (km)	3.6	2.7	2.5	4.6	4.1	5.1	5.7	7.6	3.1
ΔhMAX [σ=20 MPa] (km)	-	-	-	-	-	-	-	-	-
95% CI (km)	2.2	1.1	0.3	0.8	2.8	2.0	1.9	1.7	2.5
IQR*3 (km)	2.3	1.3	0.2	1.0	2.5	1.8	4.1	0.9	3.7
Max-Min [OE] (km)	1.8	1.2	0.1	0.6	1.3	1.4	2.0	0.6	2.6
Vol/Area (km)	3.9	0.5	0.2	1.0	2.0	-	2.0	0.9	2.0